Cell Reports

Article

Synaptotagmin-1 interacts with PI(4,5)P2 to initiate synaptic vesicle docking in hippocampal neurons

Graphical abstract

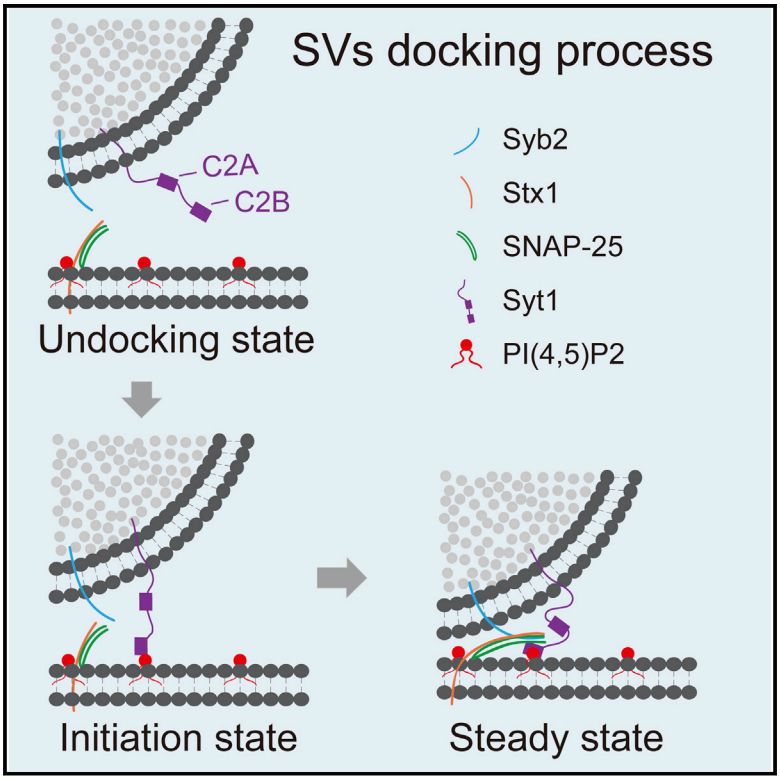

Highlights

- Syt1 corralled SVs within ~12 nm to the AZ to initiate SV docking
- PI(4,5)P2 functioned as the membrane partner of Syt1 to dock SVs
- Syt1 and PI(4,5)P2 functioned prior to the SNARE complex formation

Authors

Yun Chen, Ying-Han Wang, Yi Zheng, ..., Yao-Nan Liu, Xueming Li, Jun Yao

Correspondence

jyao@mail.tsinghua.edu.cn

In brief

Chen et al. combine TEM tomography and CRISPRi technology to demonstrate that vesicular Syt1 interacts with PI(4,5)P2 in the presynaptic plasma membrane to initiate SV docking at an ~12-nm distance to the membrane in hippocampal neurons. This process is independent of SNAREs and precedes SNARE complex formation.

Chen et al., 2021, Cell Reports *34*, 108842
March 16, 2021
https://doi.org/10.1016/j.celrep.2021.108842

CellPress

Cell Reports

CellPress
OPEN ACCESS

Article

Synaptotagmin-1 interacts with PI(4,5)P2 to initiate synaptic vesicle docking in hippocampal neurons

Yun Chen,[1,4] Ying-Han Wang,[1,4] Yi Zheng,[1,4] Meijing Li,[2] Bing Wang,[1] Qiu-Wen Wang,[1] Chong-Lei Fu,[1] Yao-Nan Liu,[1] Xueming Li,[3] and Jun Yao[1,5,*]

[1]State Key Laboratory of Membrane Biology, Tsinghua-Peking Center for Life Sciences, IDG/McGovern Institute for Brain Research, School of Life Sciences, Tsinghua University, Beijing 100084, China

[2]Max Planck Institute of Biochemistry, Department of Molecular Structural Biology, Am Klopferspitz 18, 82152 Martinsried, Germany

[3]MOE Key Laboratory of Protein Science, Advanced Innovation Center for Structural Biology, Tsinghua-Peking Center for Life Sciences, School of Life Sciences, Tsinghua University, Beijing 100084, China

[4]These authors contributed equally

[5]Lead contact

*Correspondence: jyao@mail.tsinghua.edu.cn

https://doi.org/10.1016/j.celrep.2021.108842

SUMMARY

Synaptic vesicle (SV) docking is a dynamic multi-stage process that is required for efficient neurotransmitter release in response to nerve impulses. Although the steady-state SV docking likely involves the cooperation of Synaptotagmin-1 (Syt1) and soluble *N*-ethylmaleimide-sensitive factor attachment protein receptors (SNAREs), where and how the docking process initiates remains unknown. Phosphatidylinositol-4,5-bisphosphate (PI(4,5)P2) can interact with Syt1 and SNAREs to contribute to vesicle exocytosis. In the present study, using the CRISPRi-mediated multiplex gene knockdown and 3D electron tomography approaches, we show that in mouse hippocampal synapses, SV docking initiates at ~12 nm to the active zone (AZ) by Syt1. Furthermore, we demonstrate that PI(4,5)P2 is the membrane partner of Syt1 to initiate SV docking, and disrupting their interaction could abolish the docking initiation. In contrast, the SNARE complex contributes only to the tight SV docking within 0–2 nm. Therefore, Syt1 interacts with PI(4,5)P2 to loosely dock SVs within 2–12 nm to the AZ in hippocampal neurons.

INTRODUCTION

During neuronal communication, action potential (AP)-triggered Ca^{2+} influx into the presynaptic terminals induce the fusion of synaptic vesicles (SVs) into the plasma membrane of the active zone (AZ). To fulfill the demand for efficient SV release in response to highly frequent nerve impulses in the brain, a subset of SVs is docked and further primed to the AZ membrane to form a readily releasable vesicle pool (RRP), thus becoming fusion ready (Chapman, 2008; Jahn and Fasshauer, 2012; Rosenmund and Stevens, 1996). The minimal machinery for SV fusion is composed of three soluble *N*-ethylmaleimide-sensitive factor attachment protein receptor (SNARE) proteins, including the vesicular SNARE (v-SNARE) synaptobrevin-2 (Syb2; also called VAMP2) and two target membrane SNAREs (t-SNAREs), Syntaxin-1 (Stx1) and SNAP-25 (Söllner et al., 1993; Südhof, 2013). In addition to SNAREs, the vesicular protein Synaptotagmin-1 (Syt1) acts as a primary Ca^{2+} sensor to trigger the fast synchronous phase of SV release in response to the Ca^{2+} influx (Geppert et al., 1994). Syt1 consists of a transmembrane domain and two tandem Ca^{2+}-binding C2 domains (C2A and C2B), by which it can interact with Ca^{2+}, SNAREs, and phospholipids to trigger vesicle fusion (Chapman, 2008). Because docking of SVs is presumably achieved by the direct binding of vesicular molecules to their membrane partners, both Syt1 and SNAREs have been proposed to be candidate proteins for SV docking (Neher and Brose, 2018).

SV docking is a highly dynamic process likely involving multiple stages (Neher and Brose, 2018; Park et al., 2015). In recent years, technologies such as high-pressure freezing, flash-and-freeze electron microscopy (EM), and electron tomography (ET) have been applied to research of synapses (Chang et al., 2018; Imig et al., 2014). With these tools, the distribution and translocation of SVs can be visualized at precise temporal and spatial resolutions in a near-to-native state. A number of EM studies have shown that the steady state of SV docking in neurons, which is morphologically defined as the closest attachment of SVs to the AZ membrane (e.g., <2 nm), requires the formation of the SNARE complex rather than a role for Syt1 (Arancillo et al., 2013; Geppert et al., 1994; Imig et al., 2014; Liu et al., 2009). However, whether SV docking is initiated by the assembly of SNAREs has remained contentious. A number of *in vitro* reconstitution studies have suggested that Syt1 can regulate the distance between the vesicles and target membrane according to

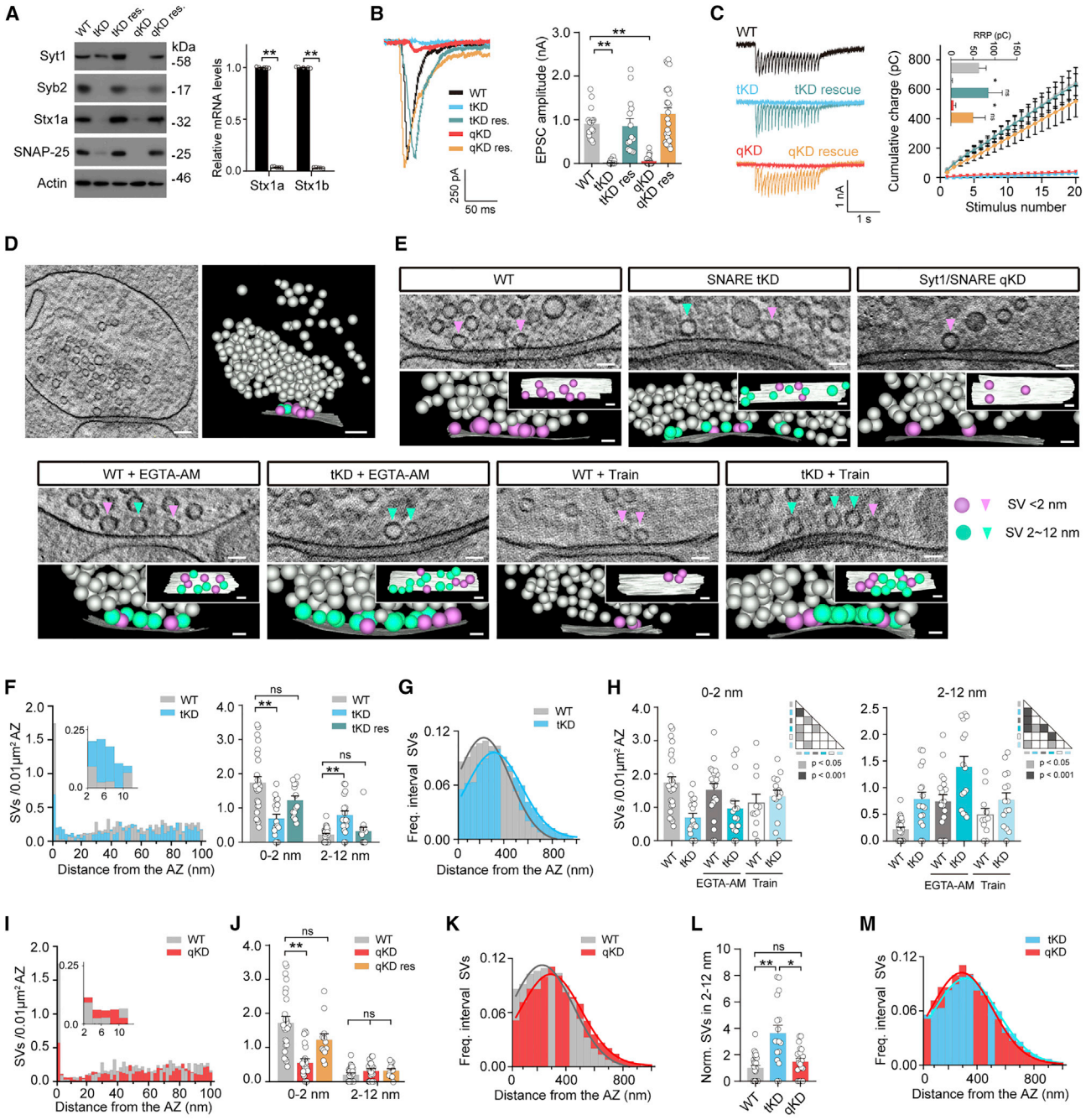

Figure 1. Vesicular Syt1 corrals SVs into the near-AZ region independent of the SNARE complex

(A) Immunoblot (left) and qRT-PCR (right) analyses of multiplex KD of SNAREs (tKD) and Syt1/SNAREs (qKD).

(B) Representative traces (left) and mean peak amplitudes (right) of single AP-evoked EPSCs recorded from WT (n = 16), tKD (n = 35), qKD (n = 30), and rescued (n = 14 for tKD; n = 26 for qKD) neurons.

(C) Representative traces (left) and cumulative charge transfer (right) of EPSCs evoked by a 2-s 10-Hz train stimulation. Bar graph (top small panel) shows summary of the readily releasable vesicle pool (RRP) size defined by y-intercepts of linear function fitted to the last 3–5 data points of EPSC trains. WT, n = 22; tKD, n = 28; qKD, n = 26; tKD rescue, n = 11; qKD rescue, n = 16.

(D) Representative electron micrograph (left) and 3D tomographic reconstruction (right) of a WT synapse. Scale bar, 100 nm.

(E) Sample micrographs (upper) and tomographic reconstructions (lower) of synapses in WT, tKD, qKD, WT + EGTA-AM, tKD + EGTA-AM, WT + Train, and tKD + Train neurons. Scale bar, 50 nm. Carmine, SVs within 0–2 nm; cyan, SVs within 2–12 nm.

(F) Spatial density analysis of SVs within 100 nm to the AZ (left) and summary of SV density within 0–2 and 2–12 nm (right) in the tKD group. WT, n = 25; tKD, n = 17; tKD rescue, n = 13.

(legend continued on next page)

the Ca^{2+} level to promote the formation of the SNARE complex and fusion of vesicles (Araç et al., 2006; Connell et al., 2008; Lin et al., 2014; van den Bogaart et al., 2011). Moreover, in neurons, neuronal activity can drive Syt1 to translocate SVs from ~5 nm to the release site (Chang et al., 2018). In addition, in PC12 cells, phosphatidylinositol-4,5-bisphosphate (PI(4,5)P2) can bind Syt1 to recruit the vesicles to the plasma membrane (Honigmann et al., 2013). These findings indicated that the Syt1-PI(4,5)P2 interaction might play a role in the tethering or docking of the SVs to the plasma membrane.

To dissect the mechanism underlying the initiation of SV docking in neurons, an ideal synaptic system should contain diverse pairing of the candidate vesicular and target membrane-docking factors, which is analogous to the *in vitro* reconstitution environment. However, this has long been challenged by the laborious and time-consuming cross-mating of multiple knockout (KO) animal models, as well as possible developmental defects and functional redundancy. In the present study, using the clustered regularly interspaced short palindromic repeats (CRISPR) interference (CRISPRi)-mediated multiplex gene knockdown (KD), high-pressure freezing, freeze substitution, and 3D ET approaches, we investigated the ignition process of SV docking within the presynaptic terminals. We demonstrated that SVs were corralled by Syt1 within a distal distance (e.g., ~12 nm) to the AZ in a resting state, representing an earliest initiation of vesicle docking. We then found that PI(4,5)P2 played a critical role in the SV docking initiation through binding to Syt1, and that disrupting their interaction could abolish the docking initiation. Finally, we showed that although the SNARE complex did not participate in the SV docking initiation process, the Syt1-PI(4,5)P2 interaction contributed to the SNARE-dependent steady-state SV docking. We therefore concluded that PI(4,5)P2 and Syt1 interacted to initiate SV docking at a ~12-nm distance to the AZ in hippocampal neurons.

RESULTS

SV docking is initiated at ~12 nm to the AZ by Syt1

SV docking at the AZ is a highly dynamic process involving multiple stages. Although the SNARE complex has been suggested to be essential for the steady-state SV docking (Imig et al., 2014), it has remained unclear where and how SV docking is initiated. This conclusion was reached largely based on neurons with only one gene deleted, which often generated controversial findings that are difficult to reconcile. In addition, SV exocytosis and animal developmental defects could also be factors affecting the number of SVs docked at the AZ. Thus, the whole picture of the docking procedure has not yet been delineated. To understand the orchestration that the molecular engine performed to initiate SV docking, we employed multiplex CRISPRi tools to achieve simultaneous inactivation of proteins likely involved in SV docking, including Syt1 and SNAREs, in 14–17 days *in vitro* (DIV) cultured mouse hippocampal neurons (Chang et al., 2018; Imig et al., 2014; Zheng et al., 2018). In the CRISPRi system, the nuclease null form Cas9 (dCas9) is fused to the transcription repressor KRAB (dCas9-KRAB) to block gene transcription. The avoidance of indels guarantees the genotypic consistency of neurons following gene suppression, thus making CRISPRi particularly suitable for inactivating genes in the brain.

We first inactivated genes encoding for SNAREs, including Syb2, SNAP-25, Stx1a, and its redundant isoform Stx1b. Immunoblot and quantitative RT-PCR (qRT-PCR) analyses revealed that in cultured hippocampal neurons, the expression of Syb2, Stx1a/1b, and SNAP-25 was efficiently abolished, thus achieving the triple KD (tKD) of SNAREs (Figure 1A). Moreover, the loss of SNAREs could be rescued by lentiviral re-introduction of exogenous cDNAs. We then performed whole-cell patch-clamp recordings in the SNARE tKD neurons to investigate the AP-evoked excitatory postsynaptic currents (EPSCs) (Figure 1B). The results indicated that the amplitude of the EPSCs was abolished in the SNARE tKD neurons compared with the wild-type (WT) group. We also tested the EPSCs evoked by a short AP train (20 stimuli at 10 Hz) and observed that the charge transfer of the EPSCs was abolished in the SNARE tKD neurons (Figure 1C). The analysis of RRP indicated that compared with the WT control, the SNARE tKD largely reduced the RRP size. Moreover, the defective EPSCs and RRP could be rescued by the expression of exogenous SNARE cDNAs.

We then carried out EM analysis to visualize the docking of SVs in the absence of SNAREs. We used the high-pressure freezing and freeze substitution approaches to preserve the near-to-native cellular structure and used the 3D ET technique to analyze the morphological distribution of SVs within a presynaptic terminal (Imig et al., 2014) (Figures 1D, 1E, S1A and S1B). We observed that compared with the WT control, the SNARE tKD attenuated the density of SVs within 0–2 nm to the AZ membrane by more than 50%; notably, the density of SVs within 2–12 nm was remarkably increased by approximately 4-fold, which could be rescued by exogenous expression of all three SNAREs, but not by any single SNARE gene (Figures 1F, 1G, S1C, and S1D). As a result, the overall density of SVs within 0–12 nm was largely unchanged by the SNARE tKD; however, the SV densities within 0–40 and 0–100 nm were reduced (Figure S2A). We analyzed the overall distribution of total SVs in the SNARE tKD neurons and found that compared with the WT neurons, the SV distribution curve was right shifted (Figure 1G),

(G) Global SV distribution of tKD group. Black and blue curves are fitted Gaussian curve.
(H) Summary of SV density within 0–2 (left) and 2–12 nm (right) in WT (n = 25), tKD (n = 17), WT + EGTA-AM (n = 19), tKD + EGTA-AM (n = 15), WT + Train (n = 11), and tKD + Train (n = 15) neurons.
(I and J) Spatial density of SVs within 100 nm (I) and 0–2 and 2–12 nm (J) in the Syt1/SNARE qKD group. WT, n = 25; qKD, n = 20; qKD rescue, n = 12.
(K) Global SV distribution of qKD neurons. Black and red curves are fitted Gaussian curve.
(L) Parallel comparison of 2- to 12-nm SV density in the tKD and qKD neurons, normalized to WT neurons.
(M) Global SV distribution of tKD and qKD neurons. Red and blue curves are fitted Gaussian curve.
(H) ANOVA. (A–G and I–M) Student's t test, *p < 0.05, **p < 0.001; error bars, SEM.
See also Figures S1, S2, and S8.

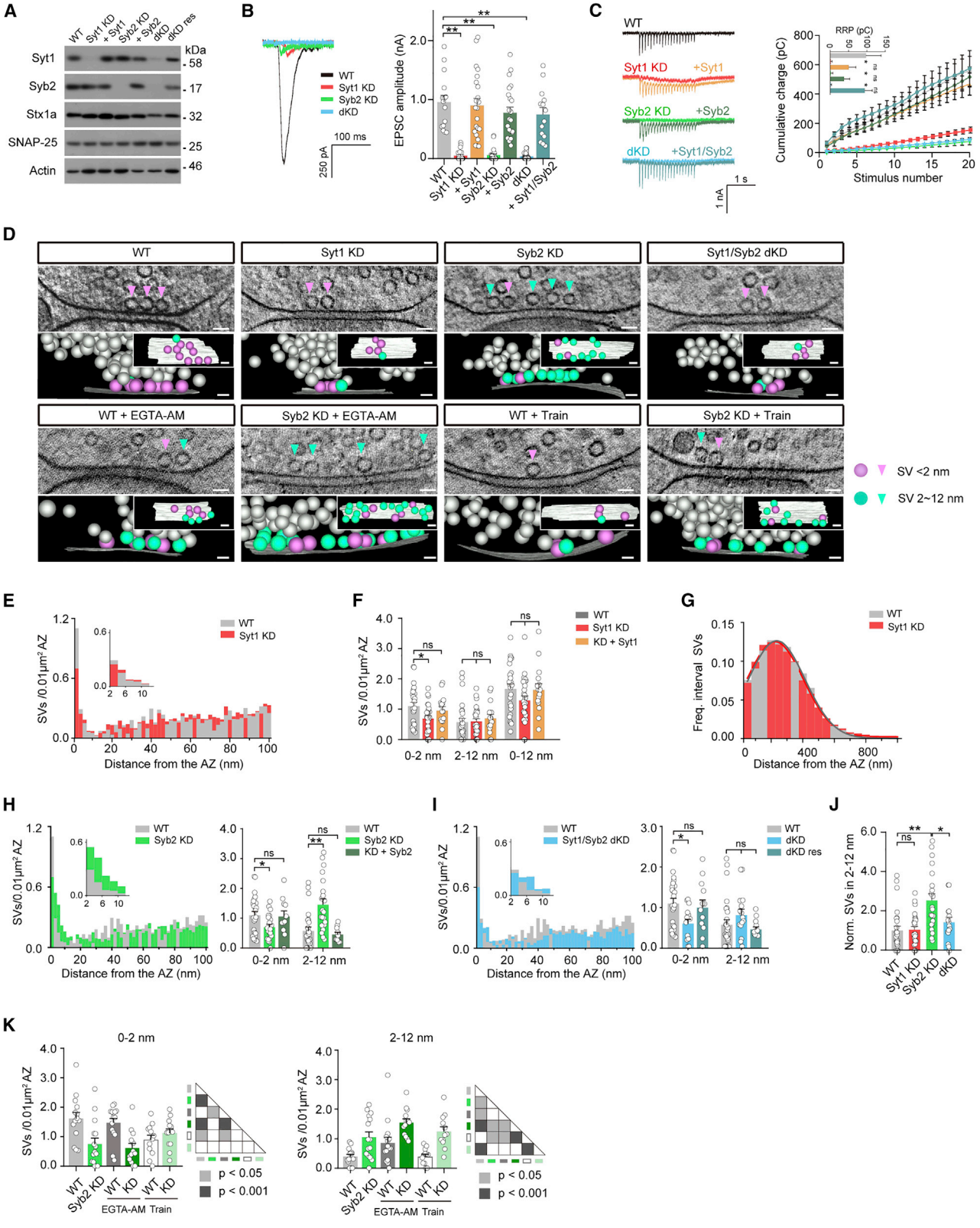

(legend on next page)

indicating that the SVs were reluctant to be transported toward the AZ. Hence the SV accumulation within 2–12 nm was unlikely caused by excess delivery of SVs to the AZ.

We also investigated the effects of different Ca^{2+} conditions on the distribution of the SVs within this range. We applied EGTA acetoxymethyl ester (EGTA-AM), a cell-permeable slow Ca^{2+} chelator, and 0 mM extracellular [Ca^{2+}] to downregulate the resting intracellular Ca^{2+} level, and a 10-s 20-Hz train stimulation (with 2 mM extracellular [Ca^{2+}]) to trigger Ca^{2+} influx (Figure 1E). In response to the train stimulation, the WT neurons showed a significantly reduced SV density within 0–2 nm but a slightly increased one within 2–12 nm, probably because the SVs were rapidly released while actively transporting toward the AZ (Figure 1H). In the tKD neurons, the train stimulation significantly increased the 0- to 2-nm SV density to the WT level, while the SV density within 2–12 nm was unaffected, indicating that SVs were delivered to the AZ membrane but could not release. Furthermore, in the WT neurons, EGTA-AM did not change the 0- to 2-nm SV density, but it induced a significant SV accumulation within 2–12 nm; in the SNARE tKD neurons, EGTA did not affect the defective 0- to 2-nm SV density, but it induced a significantly greater SV accumulation within 2–12 nm. This could be caused by saturation in the capacity of SV tightly docking within 0–2 nm. Combining the EGTA-AM and train stimulation results, it was likely that Ca^{2+} could promote the close attachment of SVs to the AZ membrane. Together, our results indicated that when SNAREs were absent, the SVs were accumulated within a 2- to 12-nm range by some mechanism to prevent their escaping from the near-AZ region.

To test the role of Syt1 in the 2- to 12-nm SV accumulation, we generated an additional Syt1-specific CRISPRi on the basis of SNARE tKD to achieve efficient quadruplex KD of Syt1 and SNAREs (Syt1/SNARE qKD), as evidenced by both immunoblot and electrophysiological analyses (Figures 1A–1C). ET analysis revealed that compared with the WT control, the SVs within 0–2 nm were reduced by more than 50%, which could be rescued by the exogenous expression of Syt1 and SNAREs, but not by any single gene (Figures 1I, 1J, and S1C); however, the SVs within 2–12 nm failed to show an obvious accumulation. Analysis of the overall SV distribution revealed that compared with the WT neurons, the densities of SVs within 0–12, 0–40, and 0–100 nm were all reduced in the qKD neurons compared with the WT controls (Figure S2A); moreover, the total SV distribution curve of the qKD neurons was right shifted (Figure 1K). We further compared the SV distribution between the SNARE tKD and Syt1/SNARE qKD neurons. The results indicated that the 2- to 12-nm SV accumulation in the SNARE tKD neurons was abolished by the additional Syt1 KD, which could be rescued when Syt1 was reintroduced (Figures 1L and S1D); moreover, the SV densities within 0–12, 0–40, and 0–100 nm were similar in the two groups of neurons (Figure S2A). Importantly, the SV distribution curve of the Syt1/SNARE qKD neurons showed a left shift compared with the SNARE tKD neurons (Figure 1M), indicating that the SV transportation could be accelerated in response to loss of Syt1. Therefore, these results indicated that the disappearance of SV accumulation induced by additional Syt1 KD was unlikely a consequence of decelerated SV transportation.

Together, our results indicated that Syt1 could act independent of the SNARE complex to corral the SVs within a ~12-nm range to the AZ.

Syt1, but not Syb2, plays a direct role in SV sequestration

Next, we asked when the SNARE proteins were present, whether Syt1 still functioned to restrict the SVs from freely escaping. We generated Syt1 single KD in WT hippocampal neurons and investigated the SV distribution. Immunoblot analysis confirmed the abolishment of Syt1 expression (Figure 2A). Consistently, patch-clamp recording analysis revealed that the amplitude and charge transfer of Syt1-triggered fast synchronous EPSCs were largely diminished in the Syt1 KD neurons (Figures 2B and 2C). Moreover, loss of Syt1 led to a significantly reduced RRP size, which is consistent with previous research in Syt1 KO neurons (Liu et al., 2009). We then carried out ET analysis and found that compared with the WT control, the Syt1 KD neurons showed a significant reduction in the density of SVs within 0–2 nm but did not show any obvious SV accumulation within 2–12 nm (Figures 2D–2F), which is in line with previous findings (Chang et al., 2018; Imig et al., 2014). Further analysis revealed that the densities of SVs within 12, 40, and 100 nm did not show a significant difference between the WT and Syt1 KD neurons (Figures 2F and S2B). Moreover, in the Syt1 KD neurons, the

Figure 2. Syt1, but not v-SNARE, plays a direct role in SV sequestration

(A) Immunoblot showing CRISPRi-based Syt1 KD, Syb2 KD, and Syt1/Syb2 dKD.

(B) Representative traces (left) and mean peak amplitudes (right) of single AP-evoked EPSCs recorded from WT (n = 15), Syt1 KD (n = 23), Syb2 KD (n = 22), Syt1/Syb2 dKD (n = 28), and rescued neurons. Syt1 KD rescue, n = 22; Syb2 KD rescue, n = 22; dKD rescue, n = 14.

(C) Representative traces (left) and cumulative charge transfer (right) of train-stimulated EPSCs recorded from WT (n = 18), Syt1 KD (n = 27), Syb2 KD (n = 22), Syt1/Syb2 dKD (n = 27), and rescued neurons. Syt1 KD rescue, n = 20; Syb2 KD rescue, n = 20; dKD rescue, n = 11. Top small panel: bar graph summarizing the RRP size.

(D) Representative electron micrographs (upper) and tomographic reconstructions (lower) of synapses. Scale bar, 50 nm.

(E) Spatial density of SVs within 100 nm in Syt1 KD neurons. WT, n = 25; Syt1 KD, n = 26; Syt1 rescue, n = 15.

(F) Mean SV density within 0–2, 2–12, and 0–12 nm of AZ in Syt1 KD neurons.

(G) Global SV distribution in Syt1 KD neurons.

(H and I) Spatial density of SVs within 100 (left) and 12 nm (right) in Syb2 KD (H) (n = 25) and Syt1/Syb2 dKD (I) (n = 15) neurons. Syb2 rescue, n = 11; dKD rescue, n = 12.

(J) Comparison of 2- to 12-nm SV density in Syt1 KD, Syb2 KD, and Syt1/Syb2 dKD neurons, normalized to WT neurons.

(K) SV density within 0–2 (left) and 2–12 nm (right) of the AZ in WT and Syb2 KD neurons with EGTA-AM treatment or train stimulation. WT, n = 14; Syb2, n = 15; WT + EGTA-AM, n = 15; Syb2 KD + EGTA-AM, n = 13; WT + Train, n = 12; Syb2 KD + Train, n = 12.

(K) ANOVA. (A–J) Student's t test, *p < 0.05, **p < 0.001; error bars, SEM.

See also Figures S2 and S8.

overall SV distribution was slightly shifted toward the AZ (Figure 2G). Hence the Syt1 inactivation-induced attenuation of SV presence within ~12 nm to the AZ was not likely caused by a decelerated SV transportation. To further evaluate the effects of Syt1 on SV distribution, we also tested Syt1$^{\Delta C2A}$ (C2A domain removed) and Syt1$^{\Delta C2B}$ (C2B domain removed) in the Syt1/SNARE qKD neurons (Figures S3A and S3B). We found that the SV sequestration by Syt1$^{\Delta C2A}$ was promoted to a 2- to 6-nm range, becoming closer to the AZ compared with the performance of Syt1^{FL}, whereas Syt1$^{\Delta C2B}$ failed to induce SV accumulation within the 2- to 12-nm distance (Figures S3C–S3E). Hence when the C2A domain of Syt1 was deleted, the SVs would be corralled closer to the AZs.

In addition to Syt1, Syb2 is also a prominent vesicular candidate protein for SV docking. Hence we investigated the effects of CRISPRi-based Syb2 KD, both in the presence and in the absence of Syt1, on SV accumulation. Regardless of the Syt1 expression, Syb2 KD could abolish the expression of Syb2 and also largely diminish the AP-evoked EPSCs (Figures 2A–2C). ET analysis revealed that compared with the WT neurons, the Syb2 KD neurons showed a significantly decreased SV density within 0–2 nm and a largely increased one within 2–12 nm (Figure 2H), which is similar to findings in the SNARE tKD neurons and a previous study (Imig et al., 2014). In contrast, in the Syt1/Syb2 double KD (dKD) neurons, although the SV density within 0–2 nm was still much lower than in the WT neurons, the 2- to 12-nm SV density was unaffected (Figure 2I), which is similar to the results in the Syt1 KD neurons. Further parallel comparison among the Syt1 KD, Syb2 KD, and Syt1/Syb2 dKD groups revealed that the loss of Syb2, but not Syt1, induced SV accumulation within the 2- to 12-nm near-AZ region, and the additional inactivation of Syt1 based on Syb2 KD dispersed the clustering of SVs (Figure 2J). In addition, overall density analysis of SVs within 100 nm to the AZ revealed that the three groups of KD neurons largely showed similar SV densities within 12, 40, and 100 nm (Figure S2B). We also manipulated SV mobilization in the Syb2 KD neurons using the EGTA-AM and train stimulation approaches (Figure 2D). Following the train stimulation, the SV densities within 0–2 and 2–12 nm were both slightly increased compared with the non-stimulated KD neurons (Figure 2K). Furthermore, in response to the EGTA-AM treatment, the 0- to 2-nm SV density was unchanged, but the SV accumulation within 2–12 nm became greater. This result is consistent with our observation in the SNARE tKD neurons and indicated that although more SVs were transported toward the AZ, they could not stably stay at the AZ membrane and consequently were detained within 2–12 nm.

Together, our results indicated that Syt1 played a direct key role in corralling SVs within 2–12 nm to the AZ to prevent the vesicles from freely escaping. Moreover, the close association of SVs to the AZ membrane was likely achieved through interactions of proteins involving Syt1 and Syb2.

The Stx1/SNAP-25 t-SNARE complex is not required for initiation of SV docking

The t-SNAREs have been suggested to play a key role in the plasma membrane attachment of large dense-core vesicles (LDCVs) in adrenal chromaffin cells and of SVs in hippocampal neurons (de Wit et al., 2009; Imig et al., 2014). Hence we asked whether the t-SNAREs Stx1 and SNAP-25 made significant contributions to the Syt1-dependent initiation of SV docking starting at a ~12-nm distance to the AZ. We inactivated the expression of t-SNAREs separately or simultaneously (Stx1/SNAP-25 dKD) in cultured hippocampal neurons. Both Stx1a and Stx1b were inactivated to exclude possible functional redundancy. The expressions of Stx1a/1b and SNAP-25 were verified to be abolished by immunoblot and qRT-PCR analyses (Figure 3A). Furthermore, patch-clamp recording analysis revealed that the single AP and train-evoked EPSCs were greatly reduced by the Stx1/SNAP-25 KD and dKD (Figures 3B and 3C). We then carried out ET analysis to investigate the performance of the Stx1/SNAP-25 KD or dKD (Figure 3D). Compared with the WT control, all three KD/dKD groups showed approximately 40%–60% reductions in the 0- to 2-nm SV density (Figures 3E–3G). Importantly, within the 2- to 12-nm space, the KD and dKD groups showed very close SV densities, which were ~5-fold higher than in the WT neurons (Figure 3H). Further analysis revealed that compared with the WT control, the densities of SVs within 0–12, 0–40, and 0–100 nm were largely unchanged in Stx1a/1b or SNAP-25 KD neurons (Figure S2C). Moreover, the dKD neurons showed significantly reduced SV densities within 0–12 and 0–40 nm, which is consistent with our observations in the SNARE tKD neurons. Together, our results indicated that the t-SNAREs were not required for the initiation of SV docking.

Loss of Syt1-SNARE interaction does not affect Syt1-initiated SV docking

To further verify the role of t-SNAREs in the initiation of SV docking, we employed mutant proteins to abolish the interactions between t-SNAREs and Syt1. We used an *in vitro* co-sedimentation assay to investigate the function of SNARE-binding motifs located at the bottom of the C2AB domain of Syt1 (Figure S4). As previously described (Zhou et al., 2017), the mutations were introduced into two motifs in the SNARE-Syt1 interface of the C2B domain (R281, E295, Y338, R398, R399, Syt1^{Q} mutant; L387, L394, Syt1^{LLQQ} mutant) (Figure 4A). In a SNARE-free and PI(4,5)P2-bearing liposome system (PI(4,5)P2-liposome), the C2AB domain of Syt1$^{Q/LLQQ}$ (C2AB$^{Q/LLQQ}$) showed a slightly reduced PI(4,5)P2-liposome binding activity compared with the WT C2AB (Figures S4B and S4C). However, in a SNARE-bearing liposome system lacking PI(4,5)P2 (t-SNARE-liposome), C2AB$^{Q/LLQQ}$ showed a largely abolished t-SNARE-liposome binding activity compared with the WT C2AB (Figures S4D and S4E).

We next investigated the performance of Syt1$^{Q/LLQQ}$ in neurons. To maximally prevent the binding of Syt1 to the t-SNAREs, we substituted the WT SNAP-25 with a mutant form SNAP-25 (K40A/D51A/E52A/E55A/D166A, SNAP-25^{Q} mutant) to further disrupt the Syt1-SNARE primary interface (Figure 4A) (Zhou et al., 2017). Patch-clamp recording analysis revealed that compared with the WT neurons, the Syt1/SNAP-25 dKD abolished the single AP and train-evoked EPSCs, which could be rescued by exogenous expression of Syt1/SNAP-25, but not Syt1$^{Q/LLQQ}$ and SNAP-25^{Q} mutants (Figures 4B and 4C). ET analysis revealed that compared with the WT neurons, the Syt1/SNAP-25 dKD not only reduced the 0- to 2-nm SV density but also failed to induce SV accumulation within the 2- to 12-nm near-AZ region (Figures 4D–4G). Re-expressing Syt1 in these

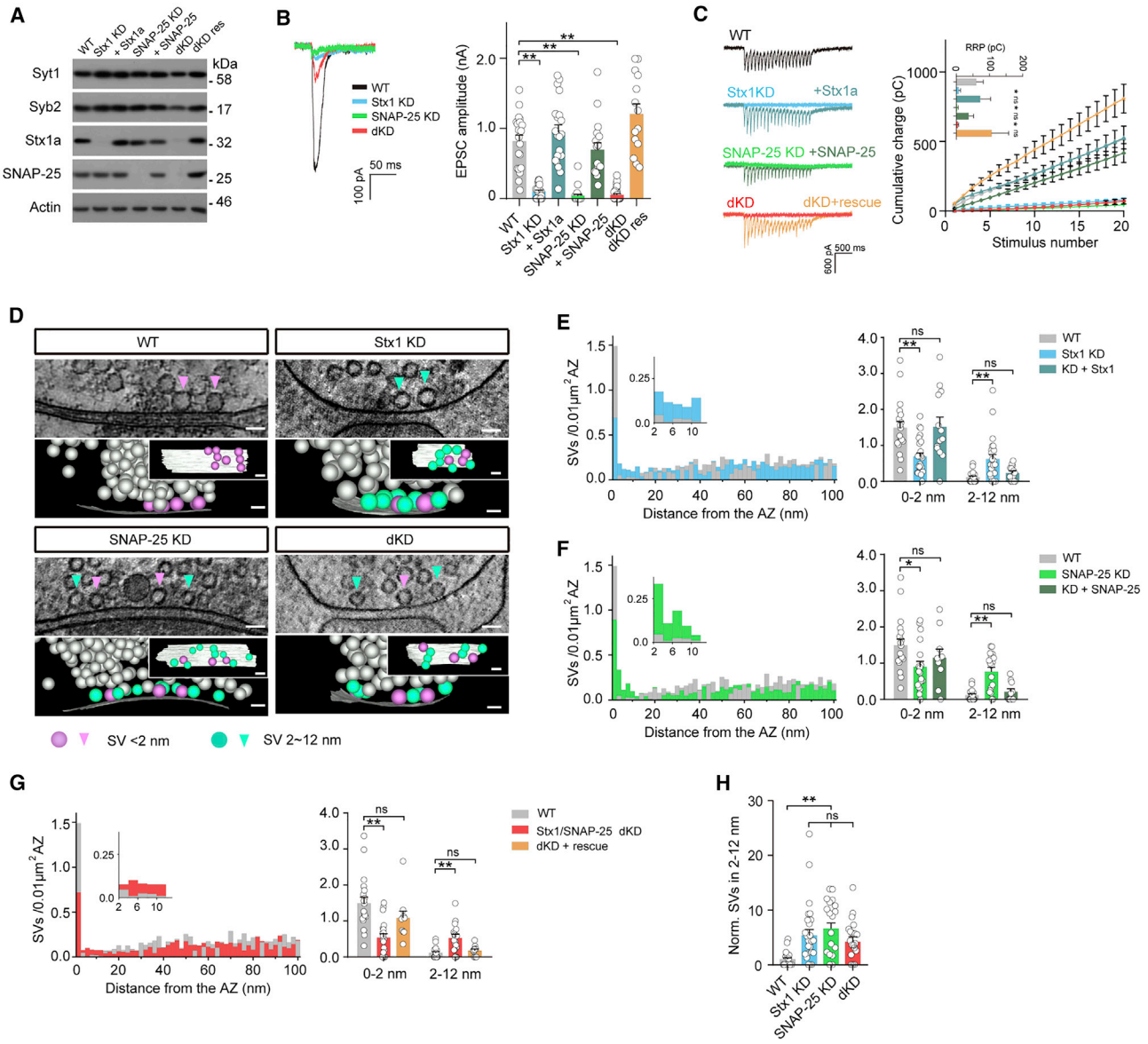

Figure 3. Removal of t-SNAREs does not affect Syt1-initiated SV docking

(A) Representative immunoblot showing CRISPRi-based Stx1 KD, SNAP-25 KD, and Stx1/SNAP-25 dKD.

(B) Representative traces (left) and mean peak amplitudes (right) of AP-evoked EPSCs recorded from WT (n = 20), Stx1 KD (n = 23), SNAP-25 KD (n = 22), Stx1/SNAP-25 dKD (n = 32), and correspondent rescued neurons. Stx1 KD rescue, n = 20; SNAP-25 KD rescue, n = 17; dKD rescue, n = 14.

(C) Representative traces (left) and cumulative charge transfer (right) of train stimulation-evoked EPSCs. WT, n = 14; Stx1 KD, n = 17; SNAP-25 KD, n = 22; Stx1/SNAP-25 dKD, n = 28; Stx1 KD rescue, n = 18; SNAP-25 KD rescue, n = 13; dKD rescue, n = 13.

(D) Sample electron micrographs (upper) and tomographic reconstructions (lower) of synapses. Scale bar, 50 nm.

(E and F) Spatial SV distribution within 100 nm (left) and mean SV density within 12 nm (right) of Stx1 KD (E) or SNAP-25 KD (F) neurons. WT, n = 19; Stx1 KD, n = 24; Stx1 KD rescue, n = 13; SNAP-25 KD, n = 18; SNAP-25 KD rescue, n = 10.

(G) 100-nm SV distribution (left) and 12-nm SV density (right) of Stx1/SNAP-25 dKD neurons. dKD, n = 20; dKD rescue, n = 10.

(H) Parallel comparison of 2- to 12-nm SV density in the synapses of Stx1 KD, SNAP-25 KD, and Stx1/SNAP-25 dKD neurons, normalized to WT neurons.

Student's t test, *p < 0.05, **p < 0.001; error bars, SEM.

See also Figures S2 and S8.

dKD neurons did not affect the defective 0- to 2-nm SV density, while it led to SV accumulation within 2–12 nm; moreover, an addition of WT SNAP-25 could fully restore the SV distribution defects in 0–2 and 2–12 nm. We then co-expressed Syt1$^{Q/LLQQ}$ and SNAP-25^{Q} in the Syt1/SNAP-25 dKD neurons (Figure 4D). The results showed that compared with the Syt1/SNAP-25 dKD neurons, the 0- to 2-nm SV density was unchanged, whereas an obvious SV accumulation was detected within 2–12 nm

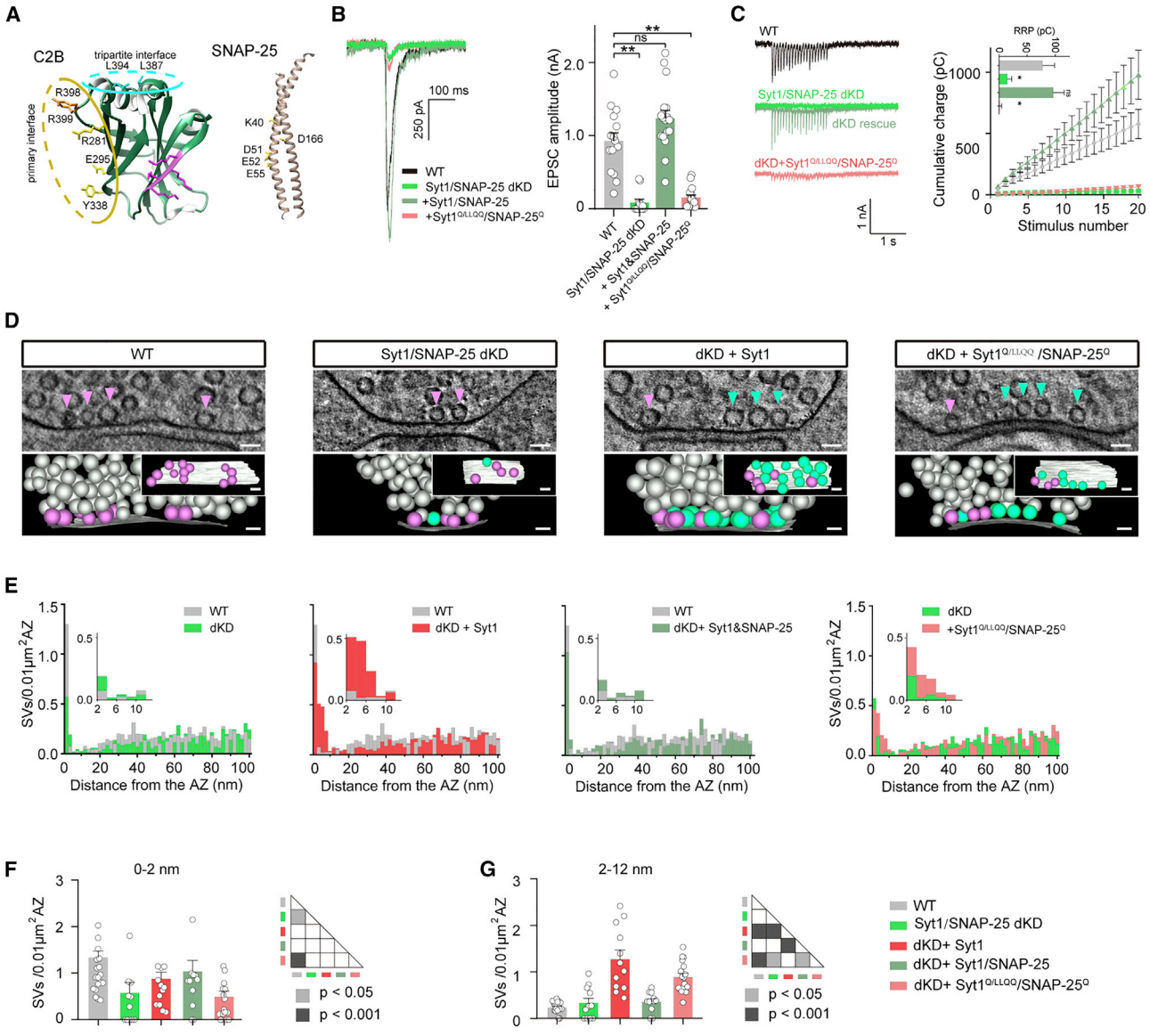

Figure 4. Syt1-SNARE binding activity is not required for Syt1 to initiate SV docking

(A) Ribbon representation of Syt1 C2B domain and SNAP-25 (accession number PDB: 5W5C). In Syt1-C2B domain, R281, E295, Y338, R398, and R399 form the primary interface between Syt1 and SNAP-25 (yellow); L387 and L394 form the tripartite interface among SNARE-Cplx-Syt1 complex (cyan). In SNAP-25, K40, D51, E52, E55, and D166 bind to Syt1. For clarity, the other components are omitted.

(B) Representative traces (left) and mean peak amplitudes (right) of AP-evoked EPSCs recorded from WT neurons (n = 15), Syt1/SNAP-25 dKD neurons (n = 12), dKD rescue neurons (n = 17), and dKD neurons expressing Syt1$^{Q/LLQQ}$/SNAP-25^{Q} (n = 15).

(C) Representative traces (left) and cumulative charge transfer (right) of train stimulation-evoked EPSCs recorded from WT neurons (n = 17), Syt1/SNAP-25 dKD neurons (n = 14), dKD rescue neurons (n = 13), and dKD neurons expressing Syt1$^{Q/LLQQ}$/SNAP-25^{Q} (n = 12).

(D) Sample electron micrographs (upper) and tomographic reconstructions (lower) of synapses. Scale bar, 50 nm.

(E) Spatial SV distribution within 100 nm to the AZ in WT, Syt1/SNAP-25 dKD, dKD + Syt1, dKD rescue neurons, and Syt1$^{Q/LLQQ}$/SNAP-25^{Q} rescue neurons. WT, n = 18; dKD, n = 11; dKD rescue, n = 11; dKD + Syt1, n = 12; Syt1$^{Q/LLQQ}$/SNAP-25^{Q}, n = 17.

(F and G) Comparison of 0–2 (F) or 2–12 nm (G) SV distribution in WT, Syt1/SNAP-25 dKD neurons, and DKD neurons expressing Syt1, Syt1/SNAP-25, or Syt1$^{Q/LLQQ}$/SNAP-25^{Q}.

(B and C) Student's t test, *p < 0.05; **p < 0.001. (F and G) ANOVA; error bars, SEM.

See also Figures S2–S5, S7, and S8.

(Figures 4E–4G), which is similar to the observations in the dKD neurons re-expressing Syt1. Further analysis revealed that compared with the WT control, this group of neurons did not show significant changes in SV density within 0–12 or 0–100 nm (Figure S2D).

Together, our results indicated that although the Syt1-SNARE binding activity of Syt1 was important for closely attaching the SVs to the AZ membrane, it was probably not required for Syt1 to initiate SV docking at ~12 nm to the AZ.

Abolishing the PI(4,5)P2 binding activity of Syt1 abolishes SV sequestration

A large amount of evidence has shown that Syt1-triggered membrane fusion requires interaction with PI(4,5)P2 via its C2B domain (Bai et al., 2004; Li et al., 2006; Radhakrishnan et al., 2009; van den Bogaart et al., 2011). Furthermore, recent *in vitro* reconstitution studies have suggested that under resting conditions, Syt1 can bind PI(4,5)P2 prior to SNARE complex formation to dock vesicles (Araç et al., 2006; Connell et al., 2008; Honigmann et al., 2013; Jahn and Fasshauer, 2012; Lin et al., 2014; Park et al., 2015; van den Bogaart et al., 2011). Hence we tested in hippocampal neurons whether the PI(4,5)P2 binding activity of Syt1 was required for Syt1 to corral SVs within 2–12 nm to the AZ membrane.

It has been found that Syt1 binds to PI(4,5)P2 through four consecutive polybasic stretches (K324–K327) in its C2B domain (Figure 5A) (Bai et al., 2004). Moreover, a recent study has suggested that substitution of K326/K327 with alanine ($Syt1^{KA}$ mutant) would not interfere with the SNARE binding activity of Syt1 (Zhou et al., 2017). We first performed the co-sedimentation assay using the C2AB domain of $Syt1^{KA}$ ($C2AB^{KA}$) (Figure S4A). In the PI(4,5)P2-liposome system, when Ca^{2+} was absent, the WT C2AB could efficiently bind to the PI(4,5)P2-liposomes in a PI(4,5)P2 dose-dependent manner, while $C2AB^{KA}$ could not effectively bind; however, in the presence of Ca^{2+}, $C2AB^{KA}$ could still efficiently bind to the PI(4,5)P2-liposomes (Figures S4B and S4C). Hence the K326/K327 site was probably required for Syt1 to bind to the target membrane under resting conditions, but not in response to Ca^{2+} influx. To test whether $C2AB^{KA}$ would interfere with Syt1-SNARE binding, we employed the PI(4,5)P2-free t-SNARE-liposome system, which was supplemented with the soluble cytosolic domain of Syb2 to facilitate SNARE complex formation (Figure S4D). We found that $C2AB^{KA}$ still largely bound to the t-SNARE-liposomes even when Ca^{2+} was absent (Figure S4E). These results are consistent with the finding in previous studies that in the presence of PI(4,5)P2, the K326/K327 site preferentially affected the PI(4,5)P2-binding activity of Syt1 rather than the SNARE-binding activity (Pérez-Lara et al., 2016; Wang et al., 2016). Hence $Syt1^{KA}$ could be used to investigate the role of Syt1-membrane binding in SV docking.

We then expressed $Syt1^{KA}$ in the Syt1-inactivated hippocampal neurons through lentiviral infection, which was confirmed by immunoblot analysis (Figure 5B). Compared with the WT and Syt1 KD groups, expression of $Syt1^{KA}$ could partially rescue the AP-evoked EPSCs in the Syt1 KD neurons (Figures 5C and 5D), which is consistent with our co-sedimentation observations and previous electrophysiological findings (Borden et al., 2005). We then performed ET analysis in the Syt1/SNARE qKD neurons to investigate the effects of $Syt1^{KA}$ on SV distribution (Figure 5E). Compared with the qKD neurons, both the Syt1- and $Syt1^{KA}$-expressing neurons showed a significantly decreased SV density within 0–2 nm; however, in the 2-to 12-nm region, $Syt1^{KA}$ failed to obviously corral SVs, which was in sharp contrast with the performance of Syt1 (Figures 5F and 5G). Further analysis revealed that compared with the qKD neurons, the $Syt1^{KA}$ expression in the qKD neurons did not show any obvious effects on SV densities within 12, 40, and 100 nm (Figure S2E). Hence $Syt1^{KA}$ could not rescue the Syt1 KD-induced deficits in SV distribution in the qKD neurons.

We also investigated the performance of $Syt1^{KA}$ in the presence of SNAREs by comparing the WT neurons and the Syt1 KD neurons expressing $Syt1^{KA}$. Compared with the WT group, expressing $Syt1^{KA}$ in the Syt1 KD neurons not only attenuated the close membrane attachment of SVs within 0–2 nm but also failed to corral SVs within 2–12 nm (Figure 5H), which is similar to our observations in the Syt1 KD neurons. Further analysis revealed that compared with the WT neurons, the $Syt1^{KA}$-expressing neurons showed reduced SV densities within 0–12 and 0–40 nm but a similar density within 0–100 nm; moreover, the total SV distribution curve was unaffected by the expression of $Syt1^{KA}$ (Figures 5I and S2F). Hence even in the presence of SNAREs, $Syt1^{KA}$ still could not corral SVs in the near-AZ region, which was unlikely caused by a decelerated SV transportation.

In addition, we tested the effects of KA mutations on neurons with Syt1/SNAP-25 replaced by $Syt1^{Q/LLQQ}$ and $SNAP\text{-}25^{Q}$ ($Syt1^{KA/Q/LLQQ}$/$SNAP\text{-}25^{Q}$). Co-sedimentation analysis confirmed that the additional KA mutations could largely weaken the PI(4,5)P2-binding activity of $C2AB^{Q/LLQQ}$ (Figures S4B–S4E). The results of ET analysis showed that the 2- to 12-nm SV accumulation in the $Syt1^{Q/LLQQ}$/$SNAP\text{-}25^{Q}$ neurons was abolished by the addition of the KA mutations (Figure S5).

Together, our results indicated that the PI(4,5)P2-binding activity was required for Syt1 to initiate SV docking within the 12-nm near-AZ region.

Manipulating PI(4,5)P2 in the AZ membrane regulates Syt1-initiated SV docking

To further test the role of PI(4,5)P2, we applied a number of approaches to modify the content of PI(4,5)P2 in the plasma membrane. First, we overexpressed a PI(4,5)P2-degrading enzyme, the membrane-targeted inositol 5-phosphatase domain of Synaptojanin-1 ($Synj^{CAAX}$), in hippocampal neurons to promote the hydrolysis of membrane-embedded PI(4,5)P2 (Krauss et al., 2003). Second, we knocked down the three isoforms (α/β/γ) of PIP5K (PIP5K tKD), which catalyze the production of PI(4,5)P2 (Tuosto et al., 2015). However, these two approaches could induce global effects in neurons. Hence in a third method, we used a group I metabotropic glutamate receptor (mGluR) agonist (S)-3,5-dihydroxyphenylglycine (DHPG) and the mGluR5 antagonist 3-((2-methyl-4-thiazolyl)ethynyl)pyridine (MTEP) to downregulate and upregulate the PI(4,5)P2, respectively, in the synapses. Immunofluorescence analysis revealed that $Synj^{CAAX}$ overexpression, PIP5K tKD, and DHPG treatment could efficiently reduce the content of PI(4,5)P2 in the neurons (Figures S6A and S6B). The analysis of super-resolution stochastic optical reconstruction microscopy (STORM) using the $Synj^{CAAX}$/PIP5K manipulated neurons revealed that the

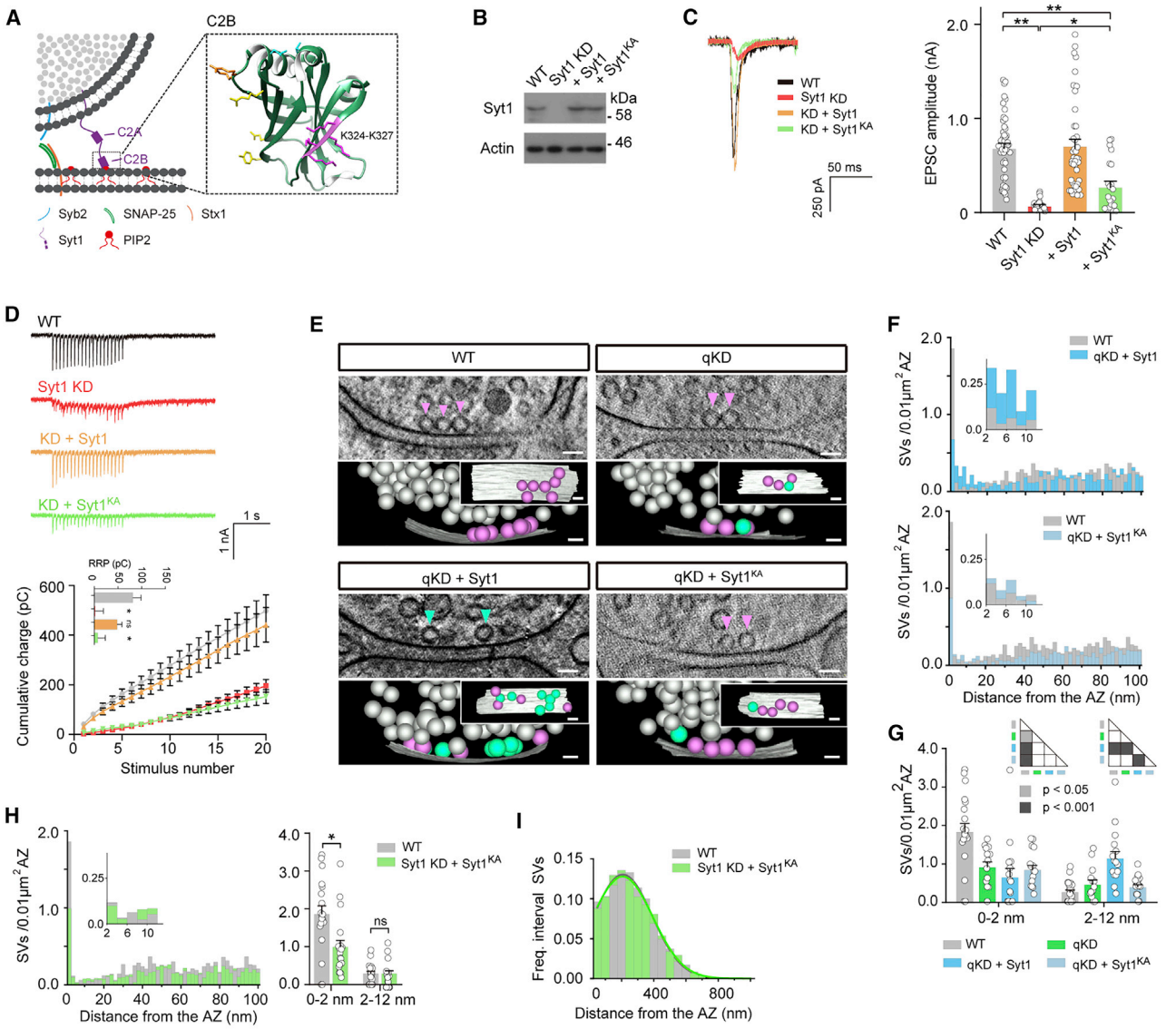

Figure 5. Syt1 corrals SVs through its PI(4,5)P2 binding activity

(A) Schematic illustration of Syt1 binding to the PI(4,5)P2 in the plasma membrane. Right: ribbon representation of Syt1 C2B domain (accession number PDB: 5W5C) showing four consecutive polybasic regions of Syt1 (K324–K327) form the lysine patch (magenta).

(B) Representative immunoblot showing the expression of Syt1^{KA} in Syt1 KD hippocampal neurons.

(C) Representative traces (left) and mean peak amplitudes (right) of single AP-evoked EPSCs recorded from WT neurons (n = 50), Syt1 KD neurons (n = 31), and KD neurons rescued by Syt1 (n = 42) or Syt1^{KA} (n = 22).

(D) Representative traces (upper) and cumulative charge transfer (lower) of train stimulation EPSCs recorded from WT neurons (n = 28), Syt1 KD neurons (n = 23), and KD neurons rescued by Syt1 (n = 17) or Syt1^{KA} (n = 14). Small panel shows the RRP size.

(E) Representative electron micrographs (upper) and tomographic reconstructions (lower) of synapses. Scale bar, 50 nm.

(F) Spatial density analysis of SVs within 100 nm to the AZ in Syt1/SNARE qKD neurons rescued by Syt1 (upper) or Syt1^{KA} (lower). WT, n = 19; qKD, n = 13; Syt1, n = 15; Syt1^{KA}, n = 16.

(G) Mean SV density within 0–2 and 2–12 nm of the AZ.

(H and I) Spatial SV distribution with 100 nm (H, left), SV density with 12 nm (H, right), and global distribution (I) of WT neurons (n = 19) and Syt1 KD neurons expressing Syt1^{KA} (n = 19). Scale bar, 50 nm.

(G) ANOVA. (A–F, H, and I) Student's t test, *p < 0.05, **p < 0.001; error bars, SEM.

See also Figures S2–S5, S7, and S8.

expression and clustering of Stx1a could be affected by PI(4,5)P2 modification (Figure S6C). However, this would not affect our investigation because we have known that Stx1a was not important for the initiation of SV docking. We also carried out patch-clamp recording experiments to analyze the effects of PI(4,5)P2 manipulation on evoked EPSCs. Compared with the WT control,

the Synj^{CAAX}-overexpressing neurons, the PIP5K tKD neurons, and the DHPG-treated neurons showed significantly attenuated evoked EPSCs, whereas the MTEP-treated neurons showed a slower EPSC depression (Figures S6D–S6I).

We then performed ET analysis to investigate the effects of PI(4,5)P2 manipulation on Syt1-initiated SV docking. For unknown reasons, the SNARE tKD hippocampal neurons expressing Synj^{CAAX} showed abnormal neuronal morphology (data not shown). Hence we performed PI(4,5)P2 manipulation in Syb2 KD neurons (Figures 6A and 6B), which could also display Syt1-mediated SV accumulation within 2–12 nm and did not show any obvious neurodevelopmental or neurodegenerative defects in response to PI(4,5)P2 modification. The results indicated that compared with the WT control group, all PI(4,5)P2 manipulating groups showed an obviously reduced 0- to 2-nm SV density, which was similar to our observation in the Syb2 KD neurons (Figure 6C). Moreover, the Synj^{CAAX} overexpression and PIP5K KD groups failed to induce SV accumulation within the 2- to 12-nm region, with the 0- to 12-, 0- to 40-, and 0- to 100-nm SV densities unchanged (Figure S2G). We observed that the DHPG-treated Syb2 KD neurons showed a weakened SV accumulation compared with the untreated Syb2 KD neurons, whereas the MTEP-treated neurons showed a similar level of SV accumulation compared with the untreated Syb2 KD neurons. To exclude the role of PI(4,5)P2 through SV proteins other than Syt1, we analyzed the effects of Synj^{CAAX} overexpression and PIP5K KD in Syt1 KD neurons and found that neither of the methods could change the SV distribution within 0–2 and 2–12 nm (Figures S6J and S6K). Hence these results indicated that reducing and increasing the PI(4,5)P2 content in the plasma membrane could attenuate and enhance the Syt1-initiated SV docking, respectively.

In addition, we investigated the effects of PI(4,5)P2 manipulation in the presence of Syb2, namely, in the WT neurons (Figure 6D). The results of ET analysis indicated that compared with the WT neurons, the Synj^{CAAX}-overexpressing neurons, the PIP5K tKD neurons, and the DHPG-treated neurons all showed a significantly reduced SV density within 0–2 nm and failed to induce SV accumulation within 2–12 nm, which were similar to the Syt1 KD neurons; moreover, the MTEP-treated neurons did not show any significant changes in SV distribution (Figures 6E and 6F).

Together, our results indicated that reducing the PI(4,5)P2 level could significantly attenuate the Syt1-initiated SV docking in the 2- to 12-nm near-AZ region, while increasing PI(4,5)P2 could slightly enhance SV docking.

DISCUSSION

Although the mechanism underlying the steady-state docking of SVs has been intensively investigated, where and how SV docking is initiated remains unclear. In the present study, we elucidated that in mouse hippocampal neurons, the plasma membrane PI(4,5)P2 bound to the vesicular Syt1 to initiate SV docking at a distance of ~12 nm from the AZ, which occurred prior to Syt1-SNARE interaction and SNARE complex assembly.

SVs are loosely docked within 2–12 nm and tightly docked within 0–2 nm to the AZ

SV docking involves multiple stages, and each step can be achieved by different protein complexes. Of these stages, two key ones are the initiation and the final stabilization of the SV-membrane association. In early chemical fixation-based EM studies, the membrane of the samples often showed deformation, and thus a ~30- to 50-nm distance to the membrane has had to be used to define docked vesicles, which might distort the conclusion. In recent years, with EM samples prepared via high-pressure freezing, a near-to-native state of close vesicle-membrane contact can be clearly visualized and defined as docking. With this technical progress, researchers have elucidated the critical roles of SNAREs in this state in different types of vesicles and cells, including SVs in neurons (Hammarlund et al., 2007, 2008; Imig et al., 2014; Wu et al., 2012). In the present study, consistent with these reports, we observed that the number of SVs within the 0- to 2-nm range was reduced when the SNAREs were silenced, either alone or all together. However, it is contentious regarding to what extent a distance as short as ~2 nm can represent docking. A number of *in vitro* studies have suggested that the vesicle-membrane association can start far beyond the 2-nm region (Araç et al., 2006; Connell et al., 2008; Honigmann et al., 2013; Jahn and Fasshauer, 2012; Lin et al., 2014; Min et al., 2013; Park et al., 2015; van den Bogaart et al., 2011). In support of these findings, in the present study, we observed that PI(4,5)P2 interacted with Syt1 at a distance of ~12 nm to the AZ to initiate SV docking, which is independent of the SNARE complex. We therefore concluded that SV docking was initiated at ~12 nm to the AZ by the pairing of Syt1-PI(4,5)P2 and was eventually stabilized in 0–2 nm in a SNARE-dependent manner. Namely, the docking process consists of a 2- to 12-nm loose docking and a 0- to 2-nm tight docking.

We note that the tight docking within 0–2 nm required the SNARE complex and could freely move back when the SNAREs were absent; however, because Syt1 was still linked to PIP2 at a largest distance of 12 nm, these membrane-detached SVs could not escape beyond this distance and thus were accumulating within 2–12 nm.

Role of Syt1 in SV docking

The roles of Syt1 in secretory vesicle docking have long been debated. Some EM studies have demonstrated vesicle docking defects in neurons and chromaffin cells of Syt1 KO mice, as well as in the neurons of *C. elegans* and *Drosophila* (Chang et al., 2018; de Wit et al., 2009; Jorgensen et al., 1995; Liu et al., 2009; Reist et al., 1998; Yu et al., 2013). However, such defects were thought to be caused by developmental issues, such as a reduction in either total vesicle number or overall vesicle transportation (Imig et al., 2014). In this study, we detected that Syt1 KD resulted in a reduced density of SVs in the steady docking state, which is consistent with a previous study that, however, suggested Syt1 played a dispensable role in steady-state SV docking (Imig et al., 2014). This conclusion was reached based on the observations that the SNARE KO neurons had similar amounts of SVs within a 40-nm space, whereas the Syt1 KD neurons showed an ~20% reduction, leading to an unchanged ratio of steady-state docked SVs to total vesicles within 40 nm. In the

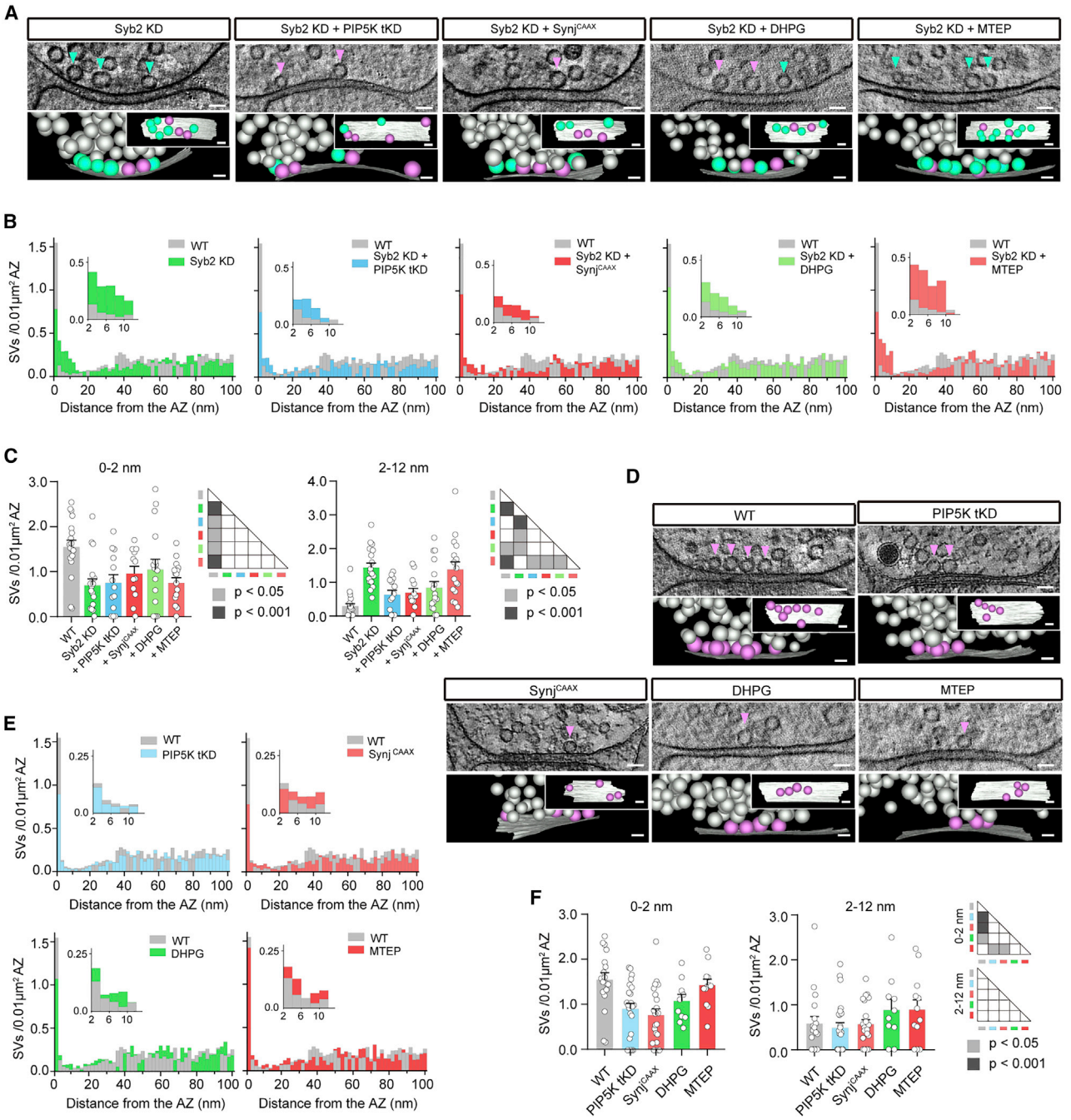

Figure 6. Manipulating PI(4,5)P2 in the AZ membrane regulates Syt1-initiated SV docking

(A) Representative electron micrographs (upper) and tomographic reconstructions (lower) of synapses in Syb2 KD neurons, and KD neurons with PIP5K tKD, Synj^{CAAX} overexpression, DHPG, or MTEP. Scale bar, 50 nm. Carmine, 0–2 nm; dark green, 2–12 nm.

(B) Spatial density analysis of SVs within 100 nm to the AZ in the synapses of WT neurons (n = 18), Syb2 KD neurons (n = 17), and KD neurons with PIP5K tKD (n = 13), Synj^{CAAX} overexpression (n = 12), and DHPG or MTEP treatment (n = 16).

(C) Mean SV density within 0–2 (left) and 2–12 nm (right) to the AZ.

(D) Sample synapses in WT neurons, and WT neurons with PIP5K tKD, Synj^{CAAX} overexpression, DHPG, or MTEP. Scale bar, 50 nm.

(E and F) Spatial density analysis of SVs within 100 (E) and 12 nm (F) to the AZ in WT neurons (n = 18) and neurons with PIP5K tKD neurons (n = 24), Synj^{CAAX} overexpression (n = 22), DHPG (n = 10), or MTEP (n = 12).

ANOVA. Error bars, SEM.

See also Figures S2 and S6–S8.

present study, we also observed that neurons with separate KD of SNAREs had unchanged densities of docked SVs at all distances, and the Syt1 KD neurons showed a slightly reduced SV density within 40 nm. However, different from the separate SNARE KD, the multiplex KD of SNAREs showed obvious reductions in the density of SVs within 0–40 and 0–100 nm, as well as a decelerated SV transportation. A likely reason for the reported reduction in 40-nm SV density in Syt1-deficient neurons was vesicle "leakage," and the results in the present study indicated that Syt1 functioned to prevent such "leakage." Moreover, inactivation of Syt1 always led to a shift of the SV distribution curve toward the AZ plasma membrane. Therefore, the Syt1 deficiency-induced SV "leakage" was not caused by defects in overall SV transportation.

PI(4,5)P2 is the membrane partner of Syt1 in SV docking under resting conditions

PI(4,5)P2 has been shown to be involved in a variety of cell functions, including vesicle exocytosis (Aoyagi et al., 2005; Brown, 2015; Cremona et al., 1999; Di Paolo et al., 2004; Koch and Holt, 2012; Milosevic et al., 2005; Wenk et al., 2001). The direct evidence that PI(4,5)P2 plays a critical role in vesicle exocytosis was provided by *in vitro* reconstitution experiments (Bai et al., 2004; Honigmann et al., 2013) and was later verified in neurons (Trexler et al., 2016). The effects of PI(4,5)P2 on vesicle trafficking could also be generated in indirect ways, such as modulating the activity of Ca^{2+} channels (Suh et al., 2010). Because PI(4,5)P2 can affect the clustering of Stx1 in the AZ, it might disturb the Stx1-involved vesicle steady-state docking, priming, and exocytosis (Ji et al., 2017; van den Bogaart et al., 2011). In the present study, we modulated the global concentration of PI(4,5)P2 using two approaches, overexpression of $Synj^{CAAX}$ and CRISPRi-based KD of PIP5K$\alpha/\beta/\gamma$ (Krauss et al., 2003; Tuosto et al., 2015). Although our STORM analysis revealed that the Stx1a clustering in the AZ was attenuated by PIP5K tKD (but was unaffected by $Synj^{CAAX}$), we later found that Stx1 was not required for the initiation of SV docking. Furthermore, we employed supplementary approaches of DHPG and MTEP to manipulate PI(4,5)P2 specifically in the synapses and observed similar docking changes. We note that even if the Stx1 clustering was maintained, these PI(4,5)P2-manipulating approaches could influence many other aspects of the dynamics of presynaptic terminals, including SV endocytosis, SV protein sorting, Ca^{2+} channel localization, and several Ca^{2+}-sensitive steps in the priming process. Therefore, our results might still be indirectly affected by these possibilities and should be combined with the investigation of Syt1 mutants to interpret the role of PI(4,5)P2.

Previously, it has been suggested that the $Syt1^{KA}$ mutant might also attenuate the SNARE-binding activity of Syt1. Interestingly, this effect was obvious only when PIP2 was absent (Rickman et al., 2004); in the presence of PI(4,5)P2, the K326/K327 site preferentially affected the PIP2- rather than SNARE-binding activity of Syt1 (Pérez-Lara et al., 2016; Wang et al., 2016). Consistent with these findings, in our co-sedimentation experiments, we observed that in the absence of PI(4,5)P2, $Syt1^{KA}$ indeed attenuated the SNARE-binding activity of Syt1, but to a much lesser extent compared with $Syt1^{Q/LLQQ}$. As a result, solely the $Syt1^{KA}$ results could not rule out the possible contribution of SNAREs to the 2- to 12-nm docking defects. However, we further observed that the $Syt1^{Q/LLQQ}$-expressing neurons, in which SNARE binding was fully abolished, showed an obvious SV accumulation within 12 nm, but to a lesser extent compared with the WT group (~30% less). This observation was sufficient to indicate that the SNAREs do not make a major contribution to SV accumulation. Because $Syt1^{Q/LLQQ}$ could slightly attenuate Syt1-PI(4,5)P2 association, it is possible that the slightly reduced PIP2 binding induced the ~30% loss of SV accumulation.

Application of multiplex CRISPRi in functional interrogation of protein complex

A good way to dissect the molecular mechanisms involved in different stages of SV docking is to test the performance of different combinations of candidate docking factors in a relatively blank environment. This strategy is commonly employed by *in vitro* reconstitution research but has been challenging for neuronal experiments because of the high cost involved and the laborious mouse strain cross-mating work and possible developmental defects or early lethality of the mice. In the present study, we used multiplex CRISPRi to achieve a near-complete inactivation of multiple genes, including Syt1, SNAREs, and PIP5K, in cultured WT hippocampal neurons. Although gene silencing in cultured neurons can be less physiologically relevant compared with brain slices, it has enabled us to largely solve issues such as developmental defects and functional redundancy in the animals. For instance, the neurons of SNAP-25 KO mice showed obvious developmental defects (Imig et al., 2014) that were not detected in the WT neurons with CRISPRi-based SNAP-25 KD. Furthermore, in Stx1a KO mice, Stx1b can likely play a redundant role to substitute Stx1a; however, mice carrying a $Stx1b^{YFP}$ mutant based on Stx1a KO showed very early lethality after birth (Arancillo et al., 2013; Bennett et al., 1992; Imig et al., 2014). Such a dilemma could be well avoided by using CRISPRi-based double KD of Stx1a/1b.

In the present study, we observed that both Syt1/PI(4,5)P2 and the SNARE complex were required for the steady-state SV docking. We have not analyzed whether other Syt1- and SNARE-interacting proteins such as Munc13/Munc18 and Complexins were involved in this process (Imig et al., 2014). Therefore, in the future, it will be necessary to carry out multiplex CRISPRi-based experiments to make clear the cooperation among these component proteins on the way to steady-state docking.

Super-resolution analysis of SV distribution

Finally, we carried out super-resolution STORM analysis to investigate SV docking in Syt1/SNARE qKD neurons expressing different Syt1 mutants. We first tested the interaction between Syt1 and PI(4,5)P2 (Figure S7A). Compared with the WT control, re-introducing Syt1 or $Syt1^{Q/LLQQ}$ into the qKD neurons did not induce any obvious changes in the shortest distance between the detected Syt1 and PI(4,5)P2 signals; in contrast, the expression of $Syt1^{KA}$ or $Syt1^{KA/Q/LLQQ}$ in the qKD neurons significantly increased the distance between Syt1 and PI(4,5)P2 (Figure S7B). Hence $Syt1^{KA}$, but not $Syt1^{Q/LLQQ}$, could attenuate the crosslinking between Syt1 and PI(4,5)P2. We then investigated the SV

distribution using vGLUT1 and Bassoon antibodies to delineate the SV cluster and AZ, respectively (Figure S7C). We found that compared with the WT control, the Syt1/SNARE qKD significantly increased the shortest distance between the SV and AZ markers, which was rescued by re-introduction of Syt1/Syt1$^{Q/LLQQ}$ but could not be restored when the KA mutation was expressed (Figure S7D). To further verify these observations, we replaced Bassoon with a PSD95 antibody to delineate the postsynaptic density (PSD) and assayed the distance between the vGLUT1 and PSD95 signals (Figure S7E). We observed identical results to the vGLUT1/Bassoon pairing experiments (Figure S7F). Together, the STORM results supported our findings in the ET analysis. However, we note that in our experiments, the shortest distance we detected between the pairing markers was often far beyond the docking window. This was probably because of the limitation in the detection of fluorescence signals and resolution of STORM technology. Moreover, we observed that the distance of the vGLUT1/Bassoon pairing was even larger than that of the vGLUT1/PSD95 pairing, indicating that the quality of the antibodies was also an important factor affecting the outcome. Therefore, the STORM analysis alone was not sufficient to determine the docking process, but it could be used as a supplemental approach to strengthen our ET findings.

Concluding remarks

In the present study, we elucidated that Syt1 probably interacted with PI(4,5)P2 to initiate SV docking in mouse hippocampal synapses. Our findings can further the understanding about the molecular mechanisms underlying neurotransmitter release.

STAR★METHODS

Detailed methods are provided in the online version of this paper and include the following:

- KEY RESOURCES TABLE
- RESOURCE AVAILABILITY
  - Lead contact
  - Materials availability
  - Data and code availability
- EXPERIMENTAL MODEL AND SUBJECT DETAILS
  - Animals
  - Mouse primary neuronal culture
- METHOD DETAILS
  - Plasmid construction and sgRNA design
  - Lentivirus preparation and infection
  - Electrophysiology
  - Immunoblot analysis
  - STORM imaging
  - Immunofluorescence
  - High-pressure freezing, freeze substitution, and three-dimensional electron microscopy
  - Quantitative reverse transcription PCR
  - Protein expression and purification
  - Liposome preparation
  - Co-sedimentation assays
- QUANTIFICATION AND STATISTICAL ANALYSIS

SUPPLEMENTAL INFORMATION

Supplemental information can be found online at https://doi.org/10.1016/j.celrep.2021.108842.

ACKNOWLEDGMENTS

We thank Drs. Wenjuan Wang (Tsinghua University), Wanzhong He (NIBS), and Xun Li (Nikon Instruments) for technical advice. We thank Xiaofeng Hu and Dr. Ying Li (Tsinghua University) for technical assistance in EM experiments. This work was supported by grants from the National Key R&D Program of China (grant no. 2016YFA0101900), National Natural Science Foundation of China (grant nos. 31830038, 31771482, and 31800852), and Beijing Municipal Science and Technology Commission (grant no. Z181100001518001).

AUTHOR CONTRIBUTIONS

Y.C., Y.-H.W., Y.Z., B.W., M.L., and X.L. conducted EM experiments. Y.-H.W. and Q.-W.W. conducted patch-clamp recording experiments. Y.C. and Y.-H.W. conducted fluorescence imaging experiments. Y.Z., C.-L.F., and Y.-N.L. conducted molecular biology and biochemistry experiments. Y.C., Y.-H.W., and J.Y. analyzed the data. J.Y. designed the experiments and wrote the manuscript.

DECLARATION OF INTERESTS

The authors declare no competing interests.

Received: May 11, 2020
Revised: January 24, 2021
Accepted: February 17, 2021
Published: March 16, 2021

REFERENCES

Aoyagi, K., Sugaya, T., Umeda, M., Yamamoto, S., Terakawa, S., and Takahashi, M. (2005). The activation of exocytotic sites by the formation of phosphatidylinositol 4,5-bisphosphate microdomains at syntaxin clusters. J. Biol. Chem. *280*, 17346–17352.

Araç, D., Chen, X., Khant, H.A., Ubach, J., Ludtke, S.J., Kikkawa, M., Johnson, A.E., Chiu, W., Südhof, T.C., and Rizo, J. (2006). Close membrane-membrane proximity induced by Ca(2+)-dependent multivalent binding of synaptotagmin-1 to phospholipids. Nat. Struct. Mol. Biol. *13*, 209–217.

Arancillo, M., Min, S.W., Gerber, S., Münster-Wandowski, A., Wu, Y.J., Herman, M., Trimbuch, T., Rah, J.C., Ahnert-Hilger, G., Riedel, D., et al. (2013). Titration of Syntaxin1 in mammalian synapses reveals multiple roles in vesicle docking, priming, and release probability. J. Neurosci. *33*, 16698–16714.

Bai, J., Tucker, W.C., and Chapman, E.R. (2004). PIP2 increases the speed of response of synaptotagmin and steers its membrane-penetration activity toward the plasma membrane. Nat. Struct. Mol. Biol. *11*, 36–44.

Bennett, M.K., Calakos, N., and Scheller, R.H. (1992). Syntaxin: a synaptic protein implicated in docking of synaptic vesicles at presynaptic active zones. Science *257*, 255–259.

Borden, C.R., Stevens, C.F., Sullivan, J.M., and Zhu, Y. (2005). Synaptotagmin mutants Y311N and K326/327A alter the calcium dependence of neurotransmission. Mol. Cell. Neurosci. *29*, 462–470.

Brown, D.A. (2015). PIP2Clustering: From model membranes to cells. Chem. Phys. Lipids *192*, 33–40.

Chang, S., Trimbuch, T., and Rosenmund, C. (2018). Synaptotagmin-1 drives synchronous Ca^{2+}-triggered fusion by C_2B-domain-mediated synaptic-vesicle-membrane attachment. Nat. Neurosci. *21*, 33–40.

Chapman, E.R. (2008). How does synaptotagmin trigger neurotransmitter release? Annu. Rev. Biochem. *77*, 615–641.

Connell, E., Giniatullina, A., Lai-Kee-Him, J., Tavare, R., Ferrari, E., Roseman, A., Cojoc, D., Brisson, A.R., and Davletov, B. (2008). Cross-linking of

phospholipid membranes is a conserved property of calcium-sensitive synaptotagmins. J. Mol. Biol. *380*, 42–50.

Courtney, N.A., Briguglio, J.S., Bradberry, M.M., Greer, C., and Chapman, E.R. (2018). Excitatory and Inhibitory Neurons Utilize Different Ca^{2+} Sensors and Sources to Regulate Spontaneous Release. Neuron *98*, 977–991.e5.

Cremona, O., Di Paolo, G., Wenk, M.R., Lüthi, A., Kim, W.T., Takei, K., Daniell, L., Nemoto, Y., Shears, S.B., Flavell, R.A., et al. (1999). Essential role of phosphoinositide metabolism in synaptic vesicle recycling. Cell *99*, 179–188.

de Wit, H., Walter, A.M., Milosevic, I., Gulyás-Kovács, A., Riedel, D., Sørensen, J.B., and Verhage, M. (2009). Synaptotagmin-1 docks secretory vesicles to syntaxin-1/SNAP-25 acceptor complexes. Cell *138*, 935–946.

Di Paolo, G., Moskowitz, H.S., Gipson, K., Wenk, M.R., Voronov, S., Obayashi, M., Flavell, R., Fitzsimonds, R.M., Ryan, T.A., and De Camilli, P. (2004). Impaired PtdIns(4,5)P2 synthesis in nerve terminals produces defects in synaptic vesicle trafficking. Nature *431*, 415–422.

Geppert, M., Goda, Y., Hammer, R.E., Li, C., Rosahl, T.W., Stevens, C.F., and Südhof, T.C. (1994). Synaptotagmin I: a major Ca2+ sensor for transmitter release at a central synapse. Cell *79*, 717–727.

Hammarlund, M., Palfreyman, M.T., Watanabe, S., Olsen, S., and Jorgensen, E.M. (2007). Open syntaxin docks synaptic vesicles. PLoS Biol. *5*, e198.

Hammarlund, M., Watanabe, S., Schuske, K., and Jorgensen, E.M. (2008). CAPS and syntaxin dock dense core vesicles to the plasma membrane in neurons. J. Cell Biol. *180*, 483–491.

Honigmann, A., van den Bogaart, G., Iraheta, E., Risselada, H.J., Milovanovic, D., Mueller, V., Müllar, S., Diederichsen, U., Fasshauer, D., Grubmüller, H., et al. (2013). Phosphatidylinositol 4,5-bisphosphate clusters act as molecular beacons for vesicle recruitment. Nat. Struct. Mol. Biol. *20*, 679–686.

Imig, C., Min, S.W., Krinner, S., Arancillo, M., Rosenmund, C., Südhof, T.C., Rhee, J., Brose, N., and Cooper, B.H. (2014). The morphological and molecular nature of synaptic vesicle priming at presynaptic active zones. Neuron *84*, 416–431.

Jahn, R., and Fasshauer, D. (2012). Molecular machines governing exocytosis of synaptic vesicles. Nature *490*, 201–207.

Ji, C., Fan, F., and Lou, X. (2017). Vesicle Docking Is a Key Target of Local $PI(4,5)P_2$ Metabolism in the Secretory Pathway of INS-1 Cells. Cell Rep. *20*, 1409–1421.

Jorgensen, E.M., Hartwieg, E., Schuske, K., Nonet, M.L., Jin, Y., and Horvitz, H.R. (1995). Defective recycling of synaptic vesicles in synaptotagmin mutants of Caenorhabditis elegans. Nature *378*, 196–199.

Koch, M., and Holt, M. (2012). Coupling exo- and endocytosis: an essential role for PIP_2 at the synapse. Biochim. Biophys. Acta *1821*, 1114–1132.

Krauss, M., Kinuta, M., Wenk, M.R., De Camilli, P., Takei, K., and Haucke, V. (2003). ARF6 stimulates clathrin/AP-2 recruitment to synaptic membranes by activating phosphatidylinositol phosphate kinase type Igamma. J. Cell Biol. *162*, 113–124.

Li, L., Shin, O.H., Rhee, J.S., Araç, D., Rah, J.C., Rizo, J., Südhof, T., and Rosenmund, C. (2006). Phosphatidylinositol phosphates as co-activators of Ca2+ binding to C2 domains of synaptotagmin 1. J. Biol. Chem. *281*, 15845–15852.

Lin, C.C., Seikowski, J., Pérez-Lara, A., Jahn, R., Höbartner, C., and Walla, P.J. (2014). Control of membrane gaps by synaptotagmin-Ca2+ measured with a novel membrane distance ruler. Nat. Commun. *5*, 5859.

Liu, H., Dean, C., Arthur, C.P., Dong, M., and Chapman, E.R. (2009). Autapses and networks of hippocampal neurons exhibit distinct synaptic transmission phenotypes in the absence of synaptotagmin I. J. Neurosci. *29*, 7395–7403.

Milosevic, I., Sørensen, J.B., Lang, T., Krauss, M., Nagy, G., Haucke, V., Jahn, R., and Neher, E. (2005). Plasmalemmal phosphatidylinositol-4,5-bisphosphate level regulates the releasable vesicle pool size in chromaffin cells. J. Neurosci. *25*, 2557–2565.

Min, D., Kim, K., Hyeon, C., Cho, Y.H., Shin, Y.K., and Yoon, T.Y. (2013). Mechanical unzipping and rezipping of a single SNARE complex reveals hysteresis as a force-generating mechanism. Nat. Commun. *4*, 1705.

Neher, E., and Brose, N. (2018). Dynamically Primed Synaptic Vesicle States: Key to Understand Synaptic Short-Term Plasticity. Neuron *100*, 1283–1291.

Park, Y., Seo, J.B., Fraind, A., Pérez-Lara, A., Yavuz, H., Han, K., Jung, S.R., Kattan, I., Walla, P.J., Choi, M., et al. (2015). Synaptotagmin-1 binds to PIP(2)-containing membrane but not to SNAREs at physiological ionic strength. Nat. Struct. Mol. Biol. *22*, 815–823.

Pérez-Lara, Á., Thapa, A., Nyenhuis, S.B., Nyenhuis, D.A., Halder, P., Tietzel, M., Tittmann, K., Cafiso, D.S., and Jahn, R. (2016). $PtdInsP_2$ and PtdSer cooperate to trap synaptotagmin-1 to the plasma membrane in the presence of calcium. eLife *5*, e15886.

Radhakrishnan, A., Stein, A., Jahn, R., and Fasshauer, D. (2009). The Ca2+ affinity of synaptotagmin 1 is markedly increased by a specific interaction of its C2B domain with phosphatidylinositol 4,5-bisphosphate. J. Biol. Chem. *284*, 25749–25760.

Reist, N.E., Buchanan, J., Li, J., DiAntonio, A., Buxton, E.M., and Schwarz, T.L. (1998). Morphologically docked synaptic vesicles are reduced in synaptotagmin mutants of Drosophila. J. Neurosci. *18*, 7662–7673.

Rickman, C., Archer, D.A., Meunier, F.A., Craxton, M., Fukuda, M., Burgoyne, R.D., and Davletov, B. (2004). Synaptotagmin interaction with the syntaxin/SNAP-25 dimer is mediated by an evolutionarily conserved motif and is sensitive to inositol hexakisphosphate. J. Biol. Chem. *279*, 12574–12579.

Rosenmund, C., and Stevens, C.F. (1996). Definition of the readily releasable pool of vesicles at hippocampal synapses. Neuron *16*, 1197–1207.

Söllner, T., Bennett, M.K., Whiteheart, S.W., Scheller, R.H., and Rothman, J.E. (1993). A protein assembly-disassembly pathway in vitro that may correspond to sequential steps of synaptic vesicle docking, activation, and fusion. Cell *75*, 409–418.

Südhof, T.C. (2013). Neurotransmitter release: the last millisecond in the life of a synaptic vesicle. Neuron *80*, 675–690.

Suh, B.C., Leal, K., and Hille, B. (2010). Modulation of high-voltage activated Ca(2+) channels by membrane phosphatidylinositol 4,5-bisphosphate. Neuron *67*, 224–238.

Trexler, A.J., Sochacki, K.A., and Taraska, J.W. (2016). Imaging the recruitment and loss of proteins and lipids at single sites of calcium-triggered exocytosis. Mol. Biol. Cell *27*, 2423–2434.

Tuosto, L., Capuano, C., Muscolini, M., Santoni, A., and Galandrini, R. (2015). The multifaceted role of PIP2 in leukocyte biology. Cell. Mol. Life Sci. *72*, 4461–4474.

van den Bogaart, G., Thutupalli, S., Risselada, J.H., Meyenberg, K., Holt, M., Riedel, D., Diederichsen, U., Herminghaus, S., Grubmüller, H., and Jahn, R. (2011). Synaptotagmin-1 may be a distance regulator acting upstream of SNARE nucleation. Nat. Struct. Mol. Biol. *18*, 805–812.

Wang, S., Li, Y., and Ma, C. (2016). Synaptotagmin-1 C2B domain interacts simultaneously with SNAREs and membranes to promote membrane fusion. eLife *5*, e14211.

Weber, T., Zemelman, B.V., McNew, J.A., Westermann, B., Gmachl, M., Parlati, F., Söllner, T.H., and Rothman, J.E. (1998). SNAREpins: minimal machinery for membrane fusion. Cell *92*, 759–772.

Wenk, M.R., Pellegrini, L., Klenchin, V.A., Di Paolo, G., Chang, S., Daniell, L., Arioka, M., Martin, T.F., and De Camilli, P. (2001). PIP kinase Igamma is the major PI(4,5)P(2) synthesizing enzyme at the synapse. Neuron *32*, 79–88.

Wu, Y., Gu, Y., Morphew, M.K., Yao, J., Yeh, F.L., Dong, M., and Chapman, E.R. (2012). All three components of the neuronal SNARE complex contribute to secretory vesicle docking. J. Cell Biol. *198*, 323–330.

Yu, D.X., Marchetto, M.C., and Gage, F.H. (2013). Therapeutic translation of iPSCs for treating neurological disease. Cell Stem Cell *12*, 678–688.

Zheng, Y., Shen, W., Zhang, J., Yang, B., Liu, Y.N., Qi, H., Yu, X., Lu, S.Y., Chen, Y., Xu, Y.Z., et al. (2018). CRISPR interference-based specific and efficient gene inactivation in the brain. Nat. Neurosci. *21*, 447–454.

Zhou, Q., Zhou, P., Wang, A.L., Wu, D., Zhao, M., Südhof, T.C., and Brunger, A.T. (2017). The primed SNARE-complexin-synaptotagmin complex for neuronal exocytosis. Nature *548*, 420–425.

STAR★METHODS

KEY RESOURCES TABLE

REAGENT or RESOURCE	SOURCE	IDENTIFIER
Antibodies		
Rabbit polyclonal anti-Synaptotagmin 1	Abcam	Cat#ab131551; RRID: #AB_11157546
Rabbit polyclonal anti-VAMP2	Abcam	Cat#ab3347; RRID: #AB_2212462
Mouse monoclonal anti-SNAP-25	Synaptic Systems	Cat#111011; RRID: #AB_887794
Mouse monoclonal anti-Syntaxin 1a	Synaptic Systems	Cat#110111; RRID: #AB_887848
Mouse monoclonal anti-Actin	Abcam	Cat#ab6276; RRID: #AB_2223210
Mouse monoclonal anti-PSD 95	Merck Millipore	Cat#MAB1598; RRID: #AB_94278
Guinea pig polyclonal Anti-VGLUT-1	Synaptic Systems	Cat#135304; RRID: #AB_887878
Rabbit polyclonal Anti- Syntaxin-1A	Synaptic Systems	Cat#110302; RRID: #AB_887846
Mouse monoclonal Anti-PIP2	Abcam	Cat#ab11039; RRID: #AB_442848
Guinea pig polyclonal Anti-SV2	Synaptic Systems	Cat#119004; RRID: #AB_10894884
Mouse polyclonal anti-Bassoon antibody	Abcam	Cat#ab82958; RRID: #AB_1860018
Rabbit polyclonal anti-MAP2 antibody	Abcam	Cat#ab32454; RRID: #AB_776174
Rabbit anti-PSD95 antibody	Abcam	Cat#ab18258; RRID: AB_444362
Goat anti-mouse AleaxFlour647 antibody	Invitrogen	Cat#a32728; RRID: AB_2633277
Goat anti-Guinea pig AleaxFlour647 antibody	Invitrogen	Cat#a21450; RRID: AB_141882
Goat anti-Guinea pig AleaxFlour568 antibody	Invitrogen	Cat#a11075; RRID:AB_141954
Goat anti-mouse ATTO488 antibody	Lockland	Cat#30706
Goat anti-rabbit AleaxFlour647 antibody	Invitrogen	Cat#a31573; RRID: AB_2536183
Goat anti-rabbit AleaxFlour568 antibody	Invitrogen	Cat#a10042; RRID: AB_2534017
Chemicals, peptides, and recombinant proteins		
Tannic acid	Sigma-Aldrich	403040
1-Hexadecene	Sigma-Aldrich	H2131
Osmium Tetroxide	Ted Pella Inc.	18451
10-nm gold colloid	Ted Pella Inc.	15703
Octyl b-D-glucopyranoside	Carbosynth	DO05161
PC	Avanti	850457C
DOPS	Avanti	840035C
DOPE	Avanti	850725C
PI(4,5)P2	Avanti	850165P
NaCl	Sigma-Aldrich	746398
D-(+)-Glucose	Sigma-Aldrich	V900392
HEPES	Sigma-Aldrich	V900477
KCl	Sigma-Aldrich	746436
CaCl2	Sigma-Aldrich	793639
MgCl2	Sigma-Aldrich	449172
Potassium D-gluconate	Sigma-Aldrich	G4500
EGTA	Sigma-Aldrich	E0396
EGTA-AM	Calbiochem	99590-86-0
DHPG	Abcam	ab12007
MTEP	Abcam	ab144307
Phosphocreatine disodium salt hydrate	Sigma-Aldrich	P7936
Adenosine 5′-triphosphate magnesium salt	Sigma-Aldrich	A9187
Guanosine 5′-triphosphate sodium salt hydrate	Sigma-Aldrich	G8877

(*Continued on next page*)

Continued

REAGENT or RESOURCE	SOURCE	IDENTIFIER
NaOH	Sigma-Aldrich	795429
Neurobasal-A	GIBCO	100888022
B27	GIBCO	17504044
Penicillin Streptomycin	GIBCO	15140122
GlutaMax-I	GIBCO	35050061
Picrotoxin	AldrichCPR	R284556
Lidocaine N-ethyl bromide	Supelco	L5783
Experimental models: cell lines		
HEK293FT	Invitrogen	R70007
Experimental models: organisms/strains		
Mouse:C57BL/6	Charles River	N/A
Oligonucleotides		
sgRNA targeting Syt1: TGTAACCGGGGCAAGCCCCC	Zheng et al., 2018	N/A
sgRNA targeting Syb2: CGGCTCGCGCTGGCTCCGAC	Zheng et al., 2018	N/A
sgRNA targeting Stx1a: CATGCGCGGATGCCGCCCCG	Zheng et al., 2018	N/A
sgRNA targeting Stx1b: ATGCGGCTGCGGCACAGGGT	Zheng et al., 2018	N/A
sgRNA targeting SNAP25: AGTGGAGGAGCCGCCGGGTA	Zheng et al., 2018	N/A
sgRNA targeting Scramble (Scr): GCGCCAAACGTGCCCTGACG	Zheng et al., 2018	N/A
sgRNA targeting PIP5Kα: CCAACTCCACCGCTCGGCTC	This paper	N/A
sgRNA targeting PIP5Kβ: GGCTCCAGCACGCCGGCCGA	This paper	N/A
sgRNA targeting PIP5Kγ: GCCGCCGCCGCCGGAGCGTT	This paper	N/A
Recombinant DNA		
Lenti-Scr-GFP	Zheng et al., 2018	N/A
Lenti-Syt1-Tss149-GFP	Zheng et al., 2018	N/A
Lenti-Syb2-Tss21-GFP	Zheng et al., 2018	N/A
Lenti-Stx1a-Tss32/1b-Tss31-GFP	Zheng et al., 2018	N/A
Lenti-SNAP-25-Tss83-GFP	Zheng et al., 2018	N/A
Lenti-Syt1/Syb2 dKD-GFP	Zheng et al., 2018	N/A
Lenti-Stx1/SNAP-25 dKD-GFP	Zheng et al., 2018	N/A
Lenti-Syt1/SNARE qKD-mCherry	Zheng et al., 2018	N/A
Lenti-SNARE tKD-mCherry	This study	N/A
Lenti-PIP5Kα/β/γ-GFP	This study	N/A
Lenti-Synj-CAAX-GFP	This study	N/A
Lenti-Syt1-mCherry	This study	N/A
Lenti-Syb2-mCherry	This study	N/A
Lenti-SNAP-25-mCherry	This study	N/A
Lenti-Stx1a-mCherry	This study	N/A
Lenti-Syt1Q/LLQQ-mCherry	This study	N/A
Lenti-Syt1KA/Q/LLQQ-mCherry	This study	N/A
Lenti-SNAP-25Q-mCherry	This study	N/A
Software and algorithms		
Fiji/ImageJ	https://fiji.sc/	N/A
MATLAB R2016a	MathWorks	N/A
GraphPad Prism6	https://www.graphpad.com	N/A
NIS-Elements AR	Nikon	N/A
IMOD Version (Version 4.7)	https://bio3d.colorado.edu/imod/	N/A

RESOURCE AVAILABILITY

Lead contact

Further information and request for resources and reagents should be directed to and will be fulfilled by the lead contact, Jun Yao (jyao@mail.tsinghua.edu.cn).

Materials availability

This study did not generate new unique reagents. All key resources are listed in Key resources table. Further information and requests for resources and reagents should be directed to the lead contact.

Data and code availability

All data in this study are included in this published article and supplementary materials.

EXPERIMENTAL MODEL AND SUBJECT DETAILS

Animals

C57BL/6 mice bred at THU with guidance and approval of the Institutional Animal Care & Use Committee of Tsinghua University and the Animal Welfare and Ethics Committee of Tsinghua University (Approval ID: 15-YJ2). The mice were housed at a constant temperature under a 7:00 to 19:00 12h:12h light/dark cycle (~200 lux white ambient illumination). Both male and female mice were used for primary neuronal culture experiments.

Mouse primary neuronal culture

Mouse hippocampal neurons were dissected from newborn male and female mice and incubated in 0.25% trypsin-EDTA (Life Technologies) for 15 min at 37°C. After washing with Hank's Buffered Salt Solution plus 5 mM HEPES (Life Technologies), 20 mM D-glucose and 2% fetal bovine serum (FBS) (GIBCO), the neurons were mechanically dissociated in culture medium and plated on poly-D-lysine-coated glass coverslips at a density of 50,000-100,000 cells/cm^2. Cells were grown in Neurobasal-A medium (Life Technologies) supplemented with 2% B-27 and 2 mM glutamax (Life Technologies). Cultures were maintained at 37°C in a 5% CO_2-humidified incubator.

METHOD DETAILS

Plasmid construction and sgRNA design

Lentiviral plasmid construction and sgRNA design were performed as previously described (Zheng et al., 2018). The expression of dCas9-KRAB was driven by the EFS promoter. The TSS was identified using the FANTOM5/CAGE promoter atlas, and the sgRNAs for Syt1 and SNAREs were previously used (KEY RESOURCES TABLE). For multiplex gene targeting, individual sgRNA cassettes were assembled using the Golden Gate cloning strategy. For overexpression experiments, a bicistronic lentiviral vector system, pLox Syn-DsRed-Syn-GFP (pLox), was used by substituting either the DsRed or GFP coding sequence or both with the target cDNA sequence. For STORM and immunostaining experiments, both DsRed and GFP were excluded to avoid fluorescence overlap. For Syt1^{KA}, K326/K327 were substituted with alanine. For Syt1$^{Q/LLQQ}$, R281/E295/Y338/R398/R399/L387/L394 were substituted with A281/A295/W338/A398/A399/Q387/Q394. For SNAP-25^{Q}, K40/ D51/E52/E55/D166 was substituted with A40/ A51/A52/A55/ A166.

Lentivirus preparation and infection

Lentiviral particles were generated by cotransfecting HEK293FT cells with virus packaging vectors. HEK293FT cells were maintained in Dulbecco's modified eagle medium (DMEM) in 10% FBS, 100 units/ml streptomycin and 100 mg/ml penicillin with 2 mM glutamax (Life Technologies). Transfection was performed using PEI (Polysciences). Five hours after transfection, the medium was changed. Virus supernatant was harvested 60 h post-transfection, filtered with a 0.22 μm PVDF filter (Millipore), ultracentrifuged at 25,000 rpm using a P28S rotor (Hitachi) and stocked in a final volume of 100 μl. Virus was added to neurons at 3-5 DIV, and neurons were analyzed at 14-17 DIV. The titer of the lentivirus was at least 5.0 × 10^8 infectious units (IU) per ml.

Electrophysiology

Whole-cell recordings were performed in voltage-clamp mode using a MultiClamp 700B amplifier (Molecular Devices). Neurons were continuously perfused with a bath solution (128 mM NaCl, 30 mM glucose, 5 mM KCl, 5 mM $CaCl_2$, 1 mM $MgCl_2$, 25 mM HEPES; pH 7.3) at room temperature via a Warner (Hamden, CT) VC-6 drug delivery system. 50 μm MTEP or 100 μm DHPG was added to bath solution, if necessary. Presynaptic neurons were depolarized with a theta stimulating electrode with a voltage step from 0 V to 20-30 V for 1 ms to trigger an action potential; evoked EPSCs were recorded from postsynaptic neurons. The readily releasable vesicle pool

(RRP) size was defined by y-intercepts of linear function fitted to the last 3-5 data points of cumulative charge transfer of train stimulation (10 Hz, 2 s) evoked EPSCs. Patch pipettes were pulled from borosilicate glass and had resistances of 3-5 MΩ when filled with internal pipette solution (130 mM K-gluconate, 1 mM EGTA, 5 mM Na-phosphocreatine, 2 mM Mg-ATP, 0.3 mM Na-GTP, 5 mM QX-314, 10 mM HEPES; pH 7.3). The series resistance was typically < 15 MΩ and was partially compensated. The membrane potential was held at −70 mV. Data were acquired using pClamp10 software (Molecular Devices), sampled at 10 kHz, and filtered at 2 kHz. Offline data analysis of EPSCs was performed using Clampfit software (Molecular Devices) and presented as mean ± s.e.m.

Immunoblot analysis

Neurons were lysed in RIPA buffer (50 mM Tris-Cl, pH 8.0, 150 mM NaCl, 1% Nonidet P-40, 0.5% sodium deoxycholate and 0.1% SDS) plus a complete protease inhibitor cocktail (Roche). Lysates were centrifuged and supernatants were subjected to SDS-PAGE. The blots were developed using an ECL kit (Pierce). Protein levels were quantified by densitometry using NIH ImageJ 1.48 software. Primary antibodies were as follows: rabbit polyclonal anti-synaptotagmin 1 antibody (1:2,000, Abcam, #ab131551), rabbit polyclonal anti-VAMP2 antibody (1:2,000, Abcam, #ab3347), mouse monoclonal anti-SNAP-25 antibody (1:5,000, Synaptic Systems, #111011), mouse monoclonal anti-syntaxin-1a antibody (1:2,000, Synaptic Systems, #110111) and mouse monoclonal anti-actin antibody (1:5,000, Abcam, #ab6276).

STORM imaging

Cultured hippocampal neurons were fixed with 4% paraformaldehyde (PFA) and 0.1% glutaradehyde in phosphate-buffered saline (PBS; pH 7.4) for 10 min, followed by washing off excess PFA and reducing unreacted aldehyde groups with 0.1% sodium borohydride ($NaBH_4$) in PBS. Cells were then blocked and permeabilized in blocking buffer (3% w/v BSA, 0.2% v/v Triton X-100 in PBS) for 1 h at room temperature, followed by incubation with primary and secondary antibodies, each for 2 h at room temperature. After washing, cells were post-fixed for 10 min with 4% PFA and 0.1% glutaraldehyde in PBS and used for STORM imaging. Primary antibodies include mouse monoclonal anti-PSD95 antibody (1:300, Merck Millipore, #MAB1598), rabbit anti-PSD95 antibody (1:300, Abcam, #ab18258), Guinea pig polyclonal anti-vGLUT1 antibody (1:500, Synaptic Systems, #135304), rabbit polyclonal anti-Syntaxin-1A antibody (1:500, Synaptic Systems, #110302), mouse monoclonal anti-PI(4,5)P2 antibody (1:200, Abcam, #ab11039), rabbit polyclonal anti-Syt1 antibody (1:200, Abcam, #ab131551) and mouse polyclonal anti-Bassoon antibody (1:200, Abcam, #ab82958). Secondary antibodies include goat anti-mouse AleaxFlour647 antibody (1:500, Invitrogen, #a32728),goat anti-Guinea pig AleaxFlour647 antibody (1:500, Invitrogen, #a21450), goat anti-Guinea pig AleaxFlour568 antibody (1:750, Invitrogen, #a11075), goat anti-mouse ATTO488 antibody (1:500, Lockland, #30706), goat anti-rabbit AleaxFlour647 antibody (1:500, Invitrogen, #a31573), and goat anti-rabbit AleaxFlour568 antibody (1:500, Invitrogen, #a10042). Imaging experiments were performed using a Nikon combined Confocal A1/SIM/STORM system with four activation/imaging lasers (405 nm, 488 nm and 561 nm from Coherent, 647 nm from MPBC) and a CFI Apo SR TIRF 100X oil (NA 1.49) objective. The images were acquired with an Andor EMCCD camera iXON 897. Data analysis was performed using NIS-Elements AR (Nikon) software.

Immunofluorescence

Cultured hippocampal neurons were fixed with 4% paraformaldehyde (PFA) and 0.2% glutaraldehyde at room temperature for 15 min, permeabilized and blocked with 0.5% (v/v) Saponin in PBS (pH 7.4) containing 2% BSA at room temperature for 10 min, immunostained with primary antibodies in PBS buffer containing 0.1% (v/v) Saponin and 2% BSA overnight at 4 °C, probed with secondary antibodies in PBS buffer containing 0.1% (v/v) Saponin and 2% BSA at room temperature for 1 h, and post-fixed with 2% paraformaldehyde at room temperature for 10 min. Images were captured on a Nikon A1 confocal microscope, Data analysis was performed using NIH ImageJ 1.48 software. Primary antibodies include mouse monoclonal anti-PI(4,5)P2 antibody (1:200, Abcam, #ab11039), rabbit polyclonal anti-MAP2 antibody (1:200, Abcam, #ab32454). Secondary antibodies include goat anti-rabbit AleaxFlour568 antibody (1:500, Invitrogen, #a10042), goat anti-mouse AleaxFlour647 antibody (1:500, Invitrogen, #a32728). 100 μm DHPG or 10 μm MTEP was used to treat neurons 15 min before fixation.

High-pressure freezing, freeze substitution, and three-dimensional electron microscopy

High-pressure freezing (HPF) and freeze substitution were performed as previously described (Imig et al., 2014). Briefly, cultured neurons grown on the sapphire disks were dipped into external cryoprotectant (20% BSA in culture medium) and carefully loaded into HPF sample carriers with the surface of the neurons oriented toward the base of the aluminum planchette. Neurons were frozen using a high-pressure freezer (HPM 100 Leica) and incubated for 48 h in 0.1% tannic acid in anhydrous acetone at −90°C. Then, the samples were washed four times with acetone and fixed and contrasted by 2% OsO4 in acetone for 7 h at −90°C, followed by a temperature ramp (5°C/h) to −20°C, 16 h at −20°C, and a ramp (10°C/h) to 4°C. The samples were then washed four times in acetone, each time 15 min, warmed to room temperature, and embedded in EPON. After that, the samples were sectioned at 200 nm thickness using an Ultracut UC7 ultramicrotome (Leica) and collected onto carbon-coated 100-mesh copper grids for ET. A 10-nm gold colloid (Ted Pella Inc., #15703) was added to the two surfaces of the grids to introduce fiducial markers for tomographic reconstruction. Transmission electron microscopy (TEM) tomography data were collected by FEI TF20 operated at 200 KeV, and single-axis tilt series

were recorded from 0° to −65° and then 0° to +65° with 1° increments and binned at 29,000-fold magnifications using a Gatan Orius SC200B CCD camera. Each electron micrograph usually contained a single synapse, and excitatory synapses were included in the analyses. However, inhibitory synapses could not be completely excluded. Tomographically reconstructed volumes were analyzed using the IMOD software package. Tomographic model reconstructions were manually segmented using the 3dmod software of the IMOD package. The AZ membrane was reconstructed with open contours in consecutive tomographic sections. The SV membrane was represented schematically as spherical. The distance between the SV and the AZ was measured by calculating the distance from the outer leaflet of the SV membrane to the inner leaflet of the AZ membrane using a specially developed macro for MATLAB. The AZ area was calculated by measuring the AZ length on each consecutive slice using a specially developed macro for MATLAB and then being multiplied by the factor of 0.611 nm (voxel depth). Each representative image was binned by the factor three and was overlay of five consecutive tomographic slices, generating a 9.17-nm thick sub-volume. Representative images were overlays of five consecutive tomographic slices, generating a 14.93-nm thick sub-volume. The whole scale of ET slices for the representative synapse in Figures 1, 2, 3, 4, 5, and 6 is shown in Figure S8. In the DHPG and MTEP treated groups, 100 μm DHPG or 10 μm MTEP was used to treat the neurons 15 min before freezing. In the EGTA-AM experiments, the neurons were incubated in a bath solution (128 mM NaCl, 30 mM glucose, 5 mM KCl, 1 mM $MgCl_2$, 25 mM HEPES; pH 7.3) with 5 μm EGTA-AM. In the train stimulation experiments, the neurons were incubated in a bath solution with 2 mM $CaCl_2$. A train stimulation (10 s, 20 Hz) was applied to evoke synaptic vesicle release. Each experiment was repeated at least 3 times, and usually 5-6 presynaptic terminals per EM were photographed and analyzed.

Quantitative reverse transcription PCR

Total RNA was isolated using Trizol (Life Technologies) according to the manufacturer's instructions. cDNA was synthesized using SuperScript III Reverse Transcription Kit (Life Technologies), and quantitative reverse transcription PCR (qRT-PCR) was performed on a Bio-Rad CFX96 thermal cycler using SYBR green supermix (Bio-Rad) and gene-specific primers. The primer sequences were: Stx1a, Forward: ACGCTGTCCCGAAAGTTTGTG; Reverse: TCCAATTCCTCACTGGTCGT; Stx1b, Forward: GACCTCACGGCAGA CATCAA; Reverse: GTCCGCAGAGGAACGATTCA. Quantitative analysis was performed employing the ΔΔCT method and the GAPDH as the endogenous control.

Protein expression and purification

Soluble Syt1 C2AB (residues 96-421) and its mutants were cloned into a pET-28a vector with an N-terminal hexa-histidine tag. Bacteria were grown as above, but continued growth at 37°C for 4 h after IPTG induction. Bacteria were resuspended in buffer II (25 mM HEPES-KOH, pH 7.4, 500 mM NaCl, 10% glycerol, 20 mM imidazole, 1 mM 2-mercaptoethanol supplemented with 1mM PMSF) and sonicated (2 s on, 6 s off, 60% duty cycle for a total time of 10 min) in an ultrasonic processor (Sonics and Materials). Lysates were incubated with 1% Triton X-100 for 1 h followed by centrifugation to remove the insoluble material. The supernatant was incubated with Ni-NTA Sepharose resin (GE Healthcare) overnight. The bound protein was extensively washed with buffer II containing 1M NaCl and 50 mM imidazole and eluted with buffer II containg 500 mM imidazole. Eluted protein was dialyzed against 20 mM HEPES-KOH, 100 mM KCl, 10% glycerol and 0.1% 2-mercaptoethanol.

Full-length Syb2-His6 and SNAP-25-His6/Stx1a were expressed as described in (Weber et al., 1998). In brief, bacteria were induced with 0.5 mM IPTG at 37°C for 4 h. The pellets were resuspended and lysed with 1% Triton X-100 by three passes through a high pressure homogenizer (ATS Engineer Inc.) at 1 000 bar. The supernatant was incubated with Ni-NTA Sepharose resin (GE Healthcare) at 4°C for 2 h while nutating. The bound protein was extensively washed with buffer I containing 1% Triton X-100 and 50 mM imidazole, and then buffer I containing 1% b-OG (w/v) and 50 mM imidazole. Finally, proteins were eluted with by buffer I containing 1% b-OG (w/v) and 500 mM imidazole.

Liposome preparation

For lipids binding analysis, liposomes were prepared as previously described (Courtney et al., 2018). Lipids were purchased from Avanti Polar Lipids. In brief, lipids composed of 30% POPE, DOPS and PI(4,5)P2 were included as indicated in Figure S2 and DOPC was used as the remaining component. The lipids were evaporated under nitrogen gas and vacuumed overnight to remove residual solvent. The dried lipid films were rehydrated (25 mM HEPES pH 7.4, 100 mM KCl) and extruded through 100-nm pore size polycarbonate filter (Avanti Polar Lipids), yielding liposomes of ∼100 nm in diameter.

For liposome pulldown analysis, liposomes containing 25% DOPS without PI(4,5)P2 were used to minimize the probability of binding between Syt1 and PI(4,5)P2. Films were dissolved in 1% β-OG (w/v) with t-SNARE complex, SNAP-25 and Stx1a heterodimers. Liposomes were formed by rapid dilution, then dialyzed in the presence of the soluble cytosolic domain of Syb2 to form the membrane anchored SNARE complex with buffer (20 mM HEPES, pH 7.4, 100 mM KCl, 20 μM EGTA, 0.1% 2-mercaptoethanol) containing Amberlite XAD-2 detergent-absorbing beads to remove detergents.

Co-sedimentation assays

For lipids binding analysis, liposomes were mixed with soluble Syt1 C2AB or its variants in the presence of 0.2 mM EGTA or 1 mM CaCl2. For liposome pulldown analysis, liposomes anchored with SNARE complex were mixed with Syt1 C2AB or its variants in the

presence of 0.2 mM EGTA. Respectively, the mixture was incubated for 15 min at room temperature and centrifuged at 65,000 RPM for 35 min in a TLA-100 rotor (Beckman). The supernatant was subjected to SDS-PAGE analysis.

QUANTIFICATION AND STATISTICAL ANALYSIS

Data summation and statistical analyses were performed using Prism (GraphPad). Data are shown as mean values ± SEM. Statistical significance was evaluated using ANOVA and two-tailed unpaired Student's t test at $p < 0.05$. The analysis approaches have been justified as appropriate by previous biological studies. Data distribution was assumed to be normal, but this was not formally tested. The statistical data for all experiments are listed in Table S1.